UNIVERSITY OF CALIFORNIA, IRVINE

DEVELOPMENT OF A CARBON BLACK CO_2 CAPTURE NANOFLUID and STUDIES ON A PHOTOTHERMAL SEPARATION PROCESS

Thesis

submitted in partial satisfaction of the requirements
for the degree of

MASTER OF SCIENCE

in Chemistry
with an emphasis in Organic Chemistry

by

Samantha Anne Goetz

Thesis Committee:
Assistant Professor Aaron Esser-Kahn, Chair
Professor Kenneth Shea
Professor Zhibin Guan

2015

DEDICATION

For my family,

in recognition of

the boundless opportunities they have provided me.

TABLE OF CONTENTS

Page

LIST OF FIGURES

LIST OF TABLES

ACKNOWLEDGMENTS

With the sincerest gratitude I would like to thank my committee chair, principle investigator, and teacher, Professor Aaron Esser-Kahn, who continually encouraged me to push the boundaries intellectually and be a better scientist. Without his acknowledgment of my potential and his guidance, this thesis would have not been possible. As a result of Aaron getting together a few chemists, a physicist, and a computational biologist in one room to discuss science, I learned to approach problems with a broader perspective than that of simply an organic chemist; and for this, I will always be thankful.

I want to express my appreciation to all members of the Esser-Kahn group for their friendships and conversations. To my senpai Dr. Du Nguyen, thank you for showing me the way (especially when it involved Mathematica). A special thank you to Dr. Maya Kleiman, for all your support both in and out of lab. To Nari Ryu and Dr. Troy Moore, serious thanks for teaching me all things phonics and biology, and for always listening to my horribly told stories. To Dr. Lalisa Stutts, thank you for always giving me your honest opinion. To Kyle Brubraker, thanks for always helping me out when I needed a hand (or a ladder). To the Esser-Kahn group, I look forward to what the future brings, and wish only the best for all of you. I would also like to thank all of the graduate and undergraduate students who have made my time at University of California, Irvine more enjoyable (shout out to the Wolf Pack).

I am honored to have Professor Kenneth Shea and Professor Zhibin Guan as committee members and would like to thank them for their time and useful insights. I would also like to thank Dr. Dmitry Fishman and Dr. Qiyin Lin for training and use of the Laser Spectroscopy Facility and the Calit2 Microscopy Center at University of California, Irvine, respectively. I thank Lee Moritz at the UCI Physical Sciences Machine Shop for machining our fabrication support devices.

In addition, a huge thank you to Professor Jason Kingsbury, who first introduced me to organic chemistry, both in the classroom and in the laboratory. To Dr. Hilan Kaplan, who oversaw my first reaction, thank you so much for encouraging me to ask more questions and always greeting me with a warm welcome. Finally, the most heartfelt of thank yous to Dr. Victor Rendina. I will never be able to thank you enough for everything you have done for me and continue to do. Thank you for your unconditional love and for always believing in me.

Lastly, I would like to thank our funding sources. This work was supported by the AFOSR Young Investigator Program under FA9550-12-1-0352 and a 3M Non-Tenured Faculty Award. I was supported by the Department of Education (DoE) through the Graduate Assistance in Areas of National Need (GAANN) fellowship.

The text of Chapter 2 is a reprint of the material as it appears in Energy and Environmental Science. The co-author listed in this publication directed and supervised research which forms the basis for the dissertation.

ABSTRACT OF THE THESIS

DEVELOPMENT OF A CARBON BLACK
CO_2 CAPTURE NANOFLUID
and
STUDIES ON A PHOTOTHERMAL SEPARATION PROCESS

Samantha Anne Goetz

Master of Science in Chemistry

University of California, Irvine, 2015

Assistant Professor Aaron Esser-Kahn, Chair

Highly efficient capture technologies used to mitigate CO_2 emissions have directed the search for alternative methods with low energy consumption rates. There is an estimated 80% increase in energy cost to operate current CO_2 capture technologies. In view of that, while most work is aimed at chemical means to reduce this energy cost, we seek to harness solar energy to improve current CO_2 capture solvent desorption efficiency. Recently, we reported a new method to release CO_2 from solutions using solar energy to drive localized photothermal heating. Photothermal release of CO_2, addresses the high-energy costs associated with regenerating capture fluids. By incorporating light absorbing nanoparticles into the capture fluid and irradiating with light, 80% of the incident light energy is used in CO_2 release, rather than heating the bulk fluid. In addition to this work, we sought to understand how the mechanism of photothermal release enhances the efficiency of this process. Through covalent modification of the surface, we explore how surface charge and polarity of the nanoparticles influence the photothermal regeneration of a CO_2 capture nanofluid through decarboxylation. By incorporating sulfonamides on the surface of CB, we enhanced the photothermal separation of CO_2 from monoethanolamine by approximately 70% more than the unmodified CB.

Chapter 1

Introduction

1.1 Motivation

Escalating atmospheric carbon dioxide levels threaten climate stability, making carbon dioxide emission management a forefront global environmental concern. With an increasing world demand for energy, CO_2 levels will continue to rise, as cheap and abundant fossil fuels remain a primary source of energy for the next 20 years. [1, 2] Carbon capture and sequestration (CCS) research into efficient removal of CO_2 from post-combustion emission streams is viewed as a field with the potential means to stabilize atmospheric CO_2 levels. [3] In proposed CCS technologies, CO_2 is captured directly from industrial or utility plant exhausts, and subsequently compressed, transported, and sequestered in subterranean or submarine storage reservoirs.

Aqueous solutions of monoethanolamine (MEA) are the most widely used industrial CO_2 absorbents due to their high reactivity, low cost, and gravimetric capacity for CO_2 of around 10% by weight (Figure 1.1). [4] The first usage of MEA was introduced in the early 1930s for the sweetening flue gas (a mixture of post-combustion gases). [5, 6] However, it was only recently

that the first pilot plant using MEA for CO_2 capture was commissioned in 2006, and since then two more pilot plants have become operational, capturing up to 7.2 tons of CO_2/day (t_{CO2}). [7, 8, 9]

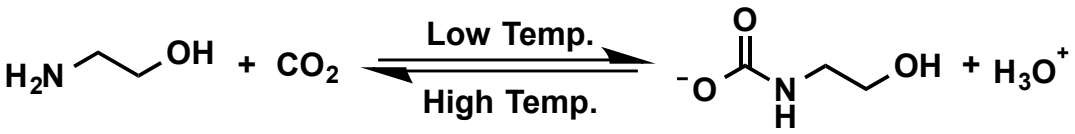

Figure 1.1: Reaction of MEA with CO_2 to form the carbamate anion.

1.2 The Post-Combustion Absorption Process

While aqueous solutions of alkanolamines are the primary CO_2 capture fluid used in post-combustion, these systems are limited in terms of sustainability. Lean MEA absorbs the CO_2, then the rich MEA is stripped of it and recycled back into the process for continuous carbon capture. In a conventional MEA-based post-combustion sorption process from a point source (Figure 1.2), flue gas CO_2 is directed to a CO_2 absorption column. There, CO_2 is absorbed by MEA to form a protonated amine and a carbamate anion according to Figure 1.1. The absorber operates at between 30 and 60 °C. Subsequently, the loaded rich solvent is transferred to the stripper, where the solution is heated to 110–130 °C, desorbing the CO_2 in a decarboxylation reaction. And finally, lean MEA is recycled back into the absorption column to restart the CO_2 capture and release.

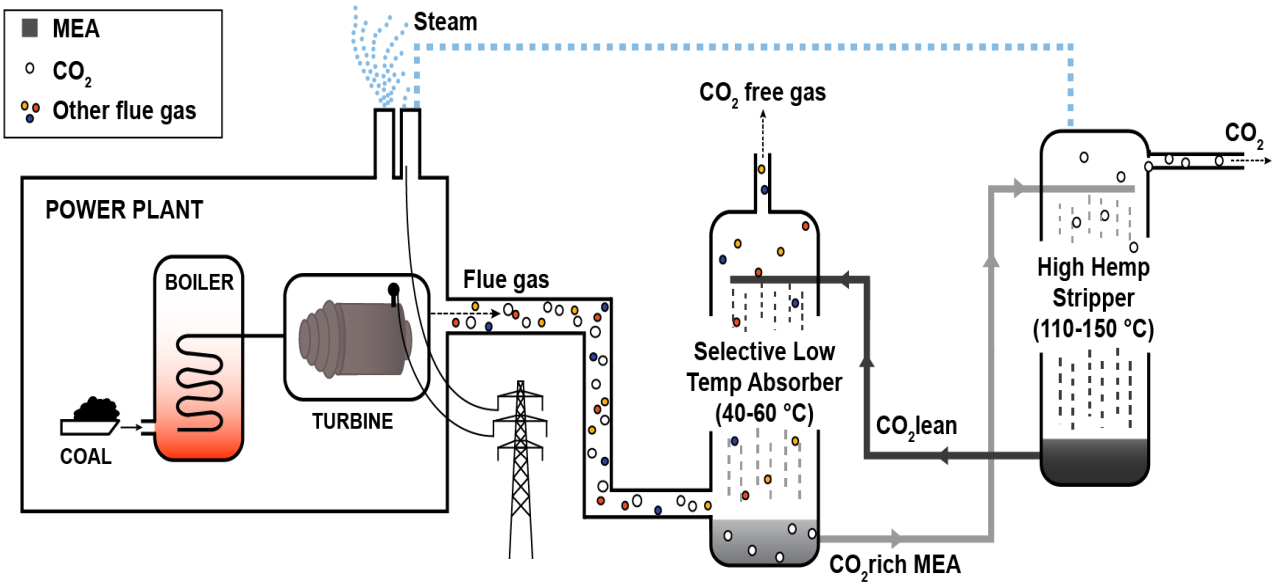

Figure 1.2: Typical MEA absorption components for pilot plant. The working temperature of the absorber and stripper respectively range between 40-60 °C and between 110-150 °C.

Thermal stripping of CO_2 from aqueous solvents occurs at temperatures greater than 100 °C, which leads to costly evaporative losses and thermal degradation due to byproduct formation. [10,11] Due to the extreme temperatures, free amine can react to form heat stable salts that reduces the available MEA for CO_2 capture. Once the solvent performance falls, additional MEA must be added to make up for the loss of reactive species. This can equate to a MEA replacement cost of up to USD \$1.2–2.3/t_{CO2} captured or between USD \$1.2 and 2.3 M per year for a plant capturing 1 million tons of CO_2 per year. [12]

This is not the only cost that hinders widespread application of this CCS technology. The energy required to regenerate MEA accounts for 80-85% of the operating cost, and additionally reduces the plant's efficiency by 30%. [12] The heat required for the high temperature stripper is usually drawn parasitically from the steam produced from the power plant itself; ideally, this steam could otherwise be sold for profit, and its reduced output results in a monetary loss. [13,14] The energy demand for this process was recorded as 2.4 GJ/t_{CO2} and a 0.3 kg/t_{CO2} MEA consumption rate. [15] A portion of the energy cost arises from the decarboxylation reaction, where 83 kJ/mol is required to break the bond between MEA and CO_2. However, the need for water as a 70 wt% co-solvent amplifies the energy requirements in stripping the CO_2 from MEA for regeneration, owing to the high specific heat of water (4.18 J g^{-1} K^{-1}). As most research in this field is designed towards decreasing the energy cost by restructuring the capture solution chemically and eliminating the need for water as a co-solvent, few methods consider coupling alternative sources of energy. One long-term goal of this work is to make the process more efficient by harnessing solar energy, to eliminate the need for energy to be drawn parasitically away from the power plant.

Chapter 2

Photothermal Separation of CO_2 from Monoethanolamine

2.1 Introduction

Solar energy has prompted notable interest for its untapped potential to provide power as a renewable resource. [16] While large-scale solar energy plants are being developed for electrical power generation, an analogous research area is in compact solar energy sources used to drive processes directly. In an effort to address the high cost and limitations of traditional carbon capture processes, broadband light absorbing nanoparticles (NPs) have emerged as promising candidates to power CO_2 release from MEA solutions through solar energy conversion.

Recently it was demonstrated that under solar illumination, NPs in water convert light to thermal energy and generate steam below 100 °C. [17, 18] By concentrating light energy into mesoscale volumes near the illuminated surface of the liquid, extreme heating at the nanoscale results in the conversion of 80% of the absorbed light energy to generate water vapor. [19, 20] It is hypothesized that the dramatic rise in temperature in the nanometer-scale vicinity of the NP is a result of dissipated Landau (nonradiative) damping, when illumination energy is not reradiated through light scattering. [21, 22] This photothermal energy has been exploited for multiple

applications ranging from cancer therapy [23, 24], laser-induced drug release [25], and nanoparticle enhanced bioimaging. [26] Nanoparticle mediated photothermal phase transitions and chemical reactions have the potential to improve many fields of energy harvesting. [27, 28, 29, 30, 31, 32, 33] Carbon nanoparticles produce strong photothermal heating effects. [34, 35]

With the intention of expanding upon this phenomenon, we incorporated carbon black nanoparticles (CB) into the aqueous MEA solution for CO_2 capture, forming a nanofluid (Figure 2.1). Upon illumination and an extreme temperature increase at the CB surface, decarboxylation is accelerated at the particle-liquid interface and CO_2 is released. CB is enveloped in a thin layer of gas with a reduced thermal conductance compared to the liquid. This insulates the nanoparticle surface and results in an increased temperature at its surface. Under continued illumination, the gas jacket volume increases and eventually moves to the liquid-air interface, where the CO_2 is released and the process is repeated. In an alternative hypothesis, the collective heating effect of the nanoparticles raises the liquid temperature to the boiling point. [36]

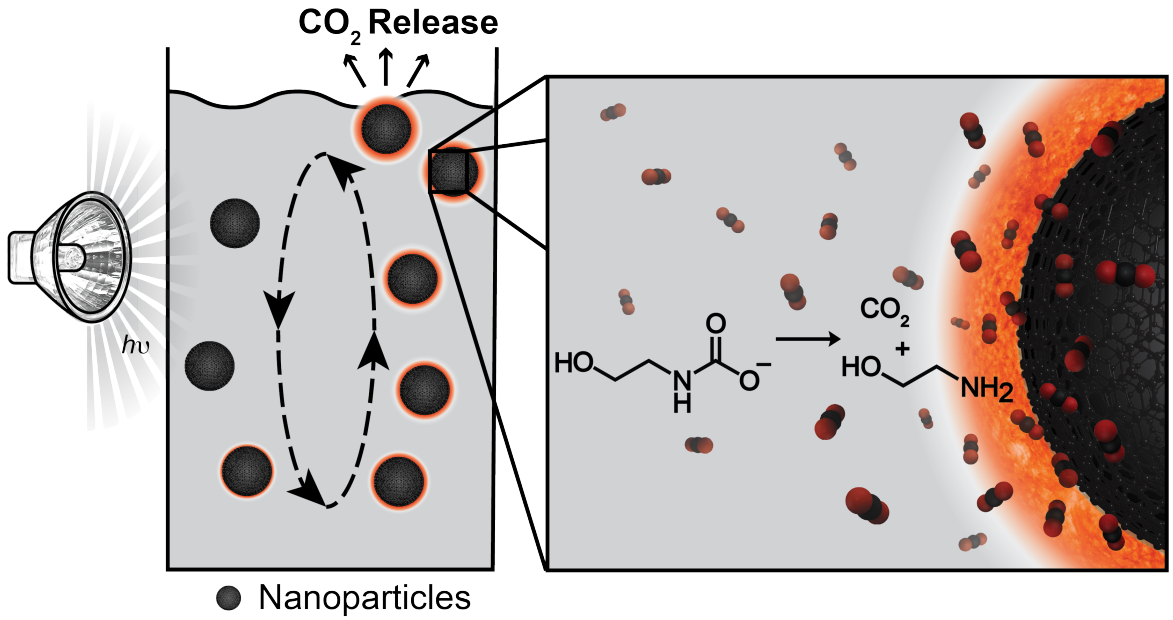

Figure 2.1: Decarboxylation of MEA using the photothermal effect of CB nanoparticles. CB concentrates incident light, resulting in a high local temperature near the nanoparticle surface. As CO_2 is released from MEA, a gas bubble grows around the nanoparticle and forces it to the surface of the fluid. The initiation of bubble growth and rate of decarboxylation may both be affected by the surface properties of CB.

In this work, we demonstrate the regeneration of a CO_2 capture-CB-nanofluid using solar energy and CO_2 stripping at bulk temperatures of 50 °C. We characterized the photothermal effect by measuring the quantity of CO_2 released with respect to the incoming actinic light. The solution regeneration efficiency of CO_2 increased with higher CB concentrations and higher initial temperatures. The regeneration process was most efficient, at 3.6 mol CO_2 released/MJ, with an initial temperature of 65 °C, using a 0.1 wt% CB, 30 wt% aqueous MEA CO_2 capture nanofluid.

2.2 Experimental

2.2.1 Materials

Commercially available carbon black nanoparticles (Cabot, Vulcan® 9 N115) were used for all experiments. Many carbon blacks exist as a range of particle sizes, aggregate sizes, and surface areas. CB N115 was chosen specifically for its widespread use in industry and in nanofluid studies. [17, 35] CB absorbs a broad range of radiant energy wavelengths, including visible and IR radiation. [35] Before use, CB was oxidized to increase its hydrophilicity. 5 g of CB was suspended in 100 mL of 30% H_2O_2, heated to 100 °C while stirring for 24 hours. The solution was then filtered and dried at 85 °C under vacuum for 24 hours. The oxidized CB was dispersed in 30 wt% MEA (40 mg in 40 mL, 4.9 M), sonicated for 20 minutes, and used as a 0.1 wt% CB capture nanofluid unless stated otherwise.

2.2.2 CO_2 Stripping Reaction Setup

A 50 mL round bottom flask containing 40 mL of the CB capture nanofluid was gravimetrically saturated with CO_2 to 10 wt% (0.5 mol CO_2/mol MEA) loading. An incoming air stream at 0.2 L/min was connected to the flask, while the reaction mixture stirred at 500 rpm. Once the light source was turned on, the photothermal release of CO_2 began instantaneously. To protect the integrity of the electronics evaporating liquids were removed from the system, and the gas stream was filtered through both condensing and drying tubes. Last, the output system air stream was monitored with an IR CO_2 meter to measure CO_2 concentration, and with a flow rate meter. Concentration and flow rate were mathematically combined to calculate the release rate of CO_2. All experiments were run in triplicate. Repeated measurements and comparisons to mass balance measurements were also conducted to validate the method (Figure 2.2b). The regeneration efficiency was measured using the CO_2 release rate and actinic light (Figure 2.2a). Light sources included LED lights or photography spotlights with powers of 0.8 W and 2.6 W respectively (incident to the flask). The refraction and Fresnel reflection of light resulted in 85% of the incident light passing into the flask. The intensity output was measured using an Ambient Weather TM-206 Solar Power Meter with a spectral sensitivity range of 400 nm to 1100 nm. Each system was characterized with respect to the amount of radiant energy required to release one mole of CO_2.

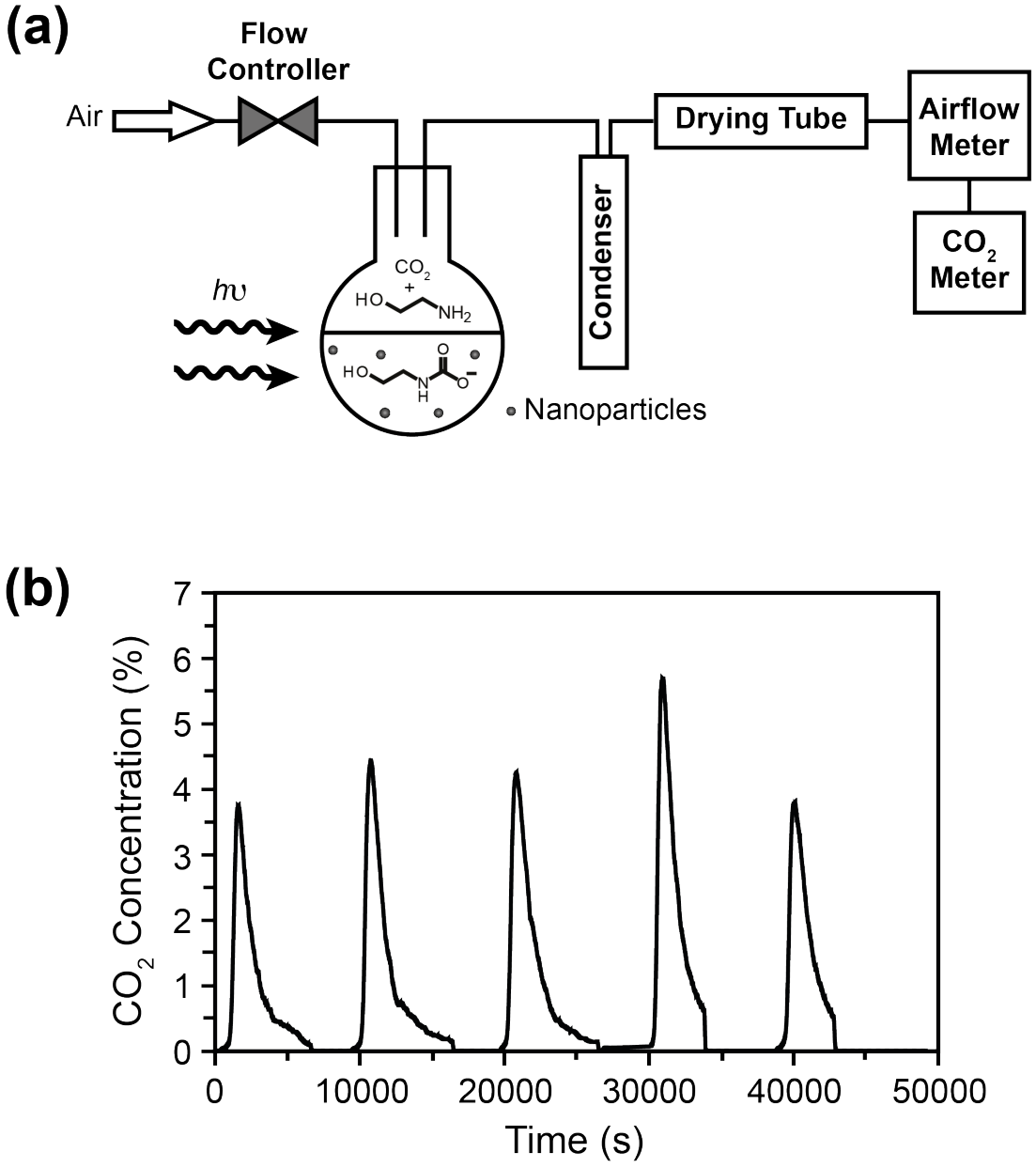

Figure 2.2: (**a**) Continuous CO_2 measurement, repeated for 5 trials, and resulting in 10% differences. (**b**) Schematic of photothermal regeneration experimental setup. In a round-bottom flask filled with aqueous MEA saturated with CO_2 and CB nanoparticles, a stream of air flows through the flask, across a condenser and drying tube, before reaching analysis instruments. Input light initiates the decarboxylation reaction, releasing CO_2, measured by the CO_2 meter. The concentration of CO_2, light irradiance, and flow rate are used to calculate the regeneration efficiency. This figure is a reprint. [37]

2.2.3 CO_2 Release Calibration

The repeatability of the photothermal CO_2 release was initially measured over the course of 5 trials using 30 wt% MEA saturated to 10 wt% CO_2 (Figure 2.2b). CB nanoparticle concentration was fixed at 0.2 wt%. Total CO_2 release was found to be within 10% uncertainty. The CO_2 mass loss from experimental data was compared to the mass loss measured by mass balance of the liquid. The difference between the values measured by the CO_2 meter and the mass balance of the liquid for all 5 runs are under 7% difference (Table 2.1). The large differences indicate that the meter measures less mass loss as compared to the mass balance. This difference could be attributed to additional loss of water that would not be measured by the CO_2 meter.

Trial	Measured CO_2 Meter	CO_2 Release Mass Balance (g)	% Difference
1	0.604	0.645	6.4
2	0.748	0.741	0.9
3	0.763	0.760	0.4
4	0.680	0.726	6.3
5	0.624	0.636	1.9

Table 2.1: Measured CO_2 results from the repeated trials using the CO_2 meter were compared to mass balance measurements. The CO_2 measurements underestimate the mass lost in comparison to the mass balance measurements due to the additional loss of water. This table is a reprint. [37]

2.3 Results and Discussion

More CO_2 was released when CB was present in the solution (Figure 2.3) and was confirmed by ^{13}C NMR (Figure 2.8). A small amount of CO_2 was also released when CB was absent from the solution. This is accounted for by two causes. First, water and glass absorb IR radiation (inherent in both solar and actinic light). This absorption results in a bulk solution temperature increase (up to 50 °C) that releases detectable amounts of CO_2. Second, the input airstream has a low partial pressure of CO_2. The low partial pressure shifts the vapor equilibrium, further releasing CO_2. When an IR filter was applied, the CO_2 concentration within the detection stream was reduced to <0.5% indicating that IR is largely responsible for background release. As a control experiment, a 50 °C water bath was used to induce the heated release of CO_2 without solar light. The total CO_2 release was similar to the aqueous MEA solution without CB, though the profiles were distinctive. A computational model* of CO_2 solubility was also used to support that photothermal release of CO_2 was not due to bulk heating or the low partial pressure of CO_2 in the stripping reaction setup. [38, 39]

* A complete discussion of this model is included in the Ph.D. dissertation of Dr. Du T. Nguyen.

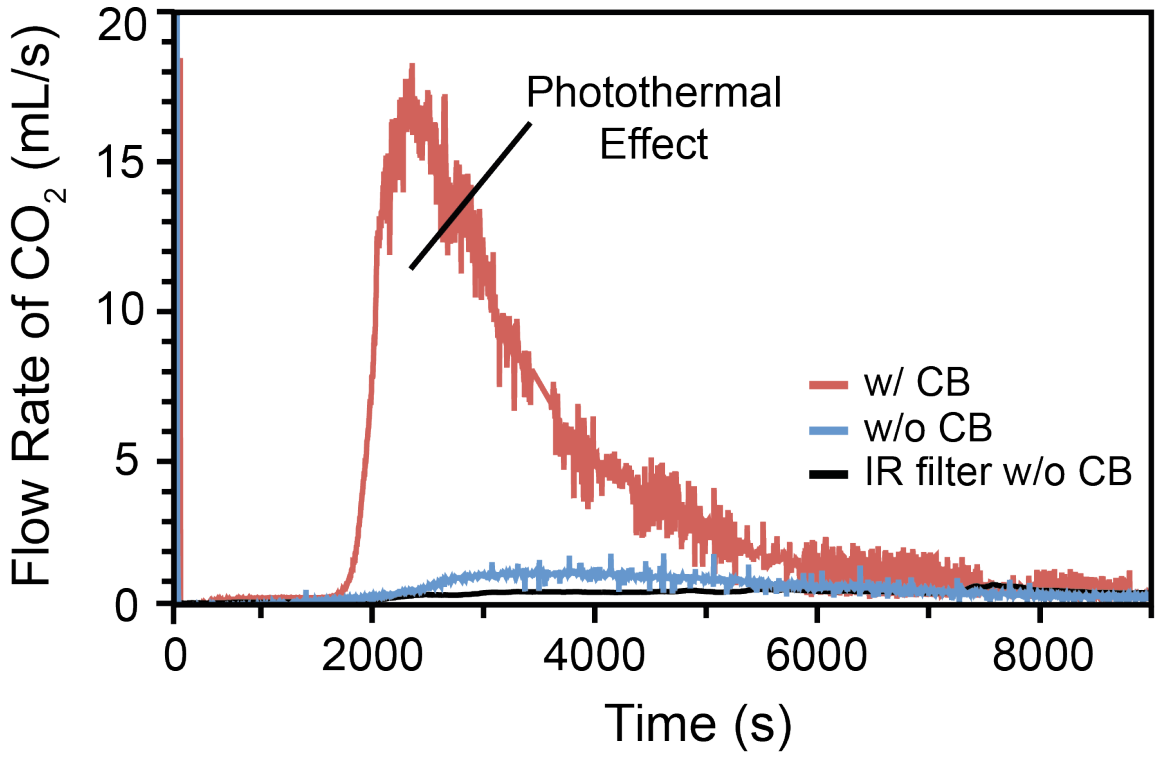

Figure 2.3: Representative data of using the photothermal effect for decarboxylation. Release of CO_2 is triggered by light in MEA. CO_2 release rate at 60 °C enhanced with CB nanoparticles in solution. After 2,000 sec, the maximum amount of CO_2 is released. Some CO_2 is released without carbon black due to the IR transmittance of the light source, resulting in increased bulk fluid temperatures.

As the CB nanoparticles enhanced release of CO_2 from MEA, we examined CO_2 release as a function of CB concentration. A 30 wt% aqueous MEA solution was used as the capture fluid, and was illuminated by the 2.6 W light source. Higher concentrations of CB resulted in higher regeneration efficiencies (Figure 2.4a). Solutions with no nanoparticles still released little CO_2, but at lower levels due to IR absorption as discussed formerly. Bulk solution temperatures reached 50 °C (Figure 2.4b). A possible explanation for the enhanced solution regeneration

efficiency at higher CB concentrations is that the increased number of nanoparticles creates a larger surface area for the localized heating and nucleation of CO_2. Concentrations above 0.15 wt% did not result in higher regeneration efficiencies. Above this concentration, all light was absorbed by the nanofluid and no further absorption occurred.

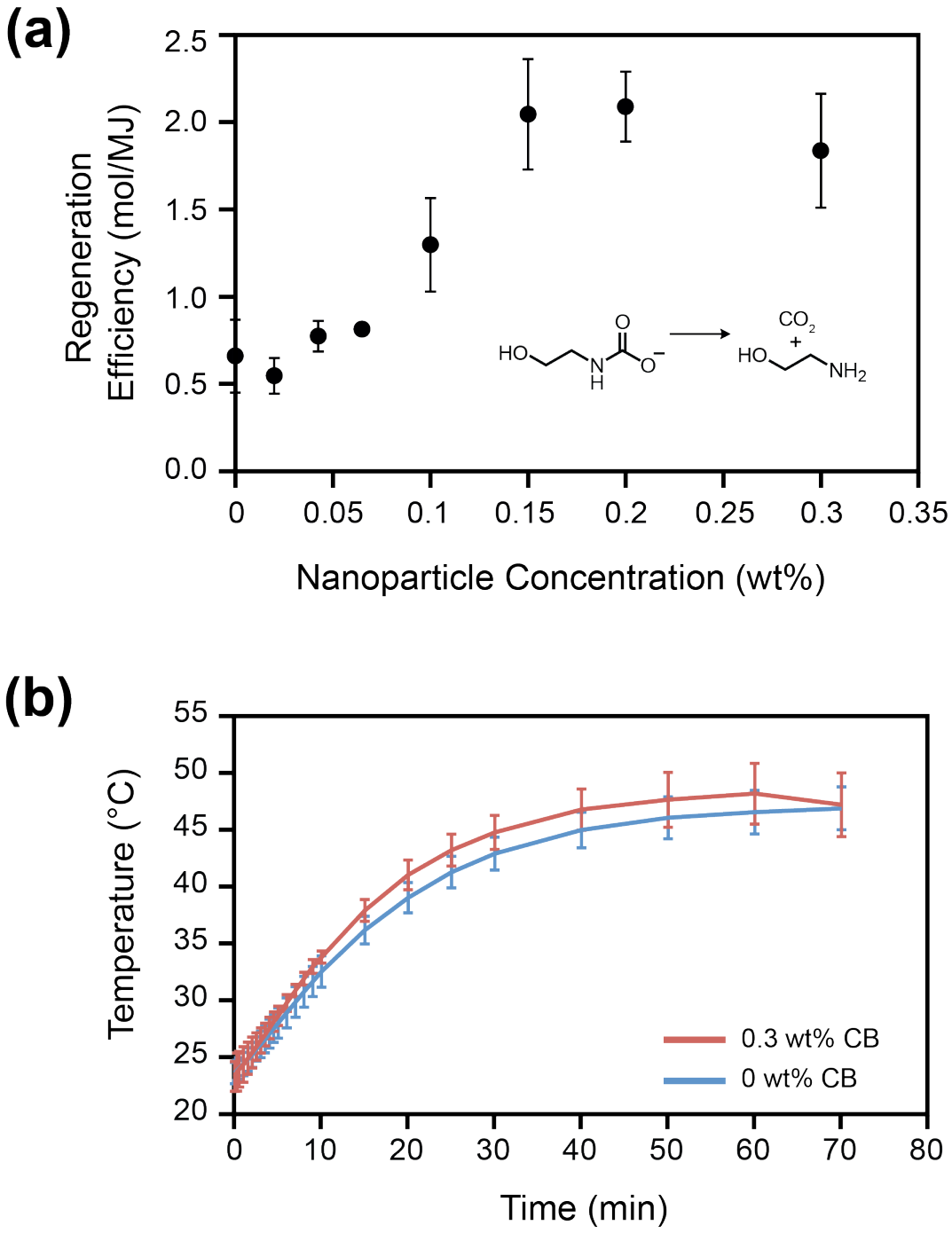

Figure 2.4: (**a**) CB nanoparticle concentration. Regeneration efficiency increased with increasing nanoparticle concentration. Bulk temperatures reached 50 °C. (**b**) Temperature evolutions, where temperature profiles were measured with respect to time at 0 wt% and 0.3 wt% CB using a thermocouple. Bulk temperatures only show minor differences. This figure is a reprint. [37]

Next, we investigated the effects of the bulk solution temperature on regeneration efficiency. In most CO_2 stripping configurations, the temperature of CO_2 rich MEA is elevated above room temperature, as the absorption reaction with CO_2 is exothermic. Here, flowing preheated water through the reaction via a circulator modulated the bulk temperature. This internal heating method was used to minimize the shading of the nanoparticle solution. As expected, higher initial temperatures resulted in increased regeneration efficiency (Figure 2.5). The largest efficiency in the scope of this report was found at 65 °C (3.6 mol CO_2/MJ).

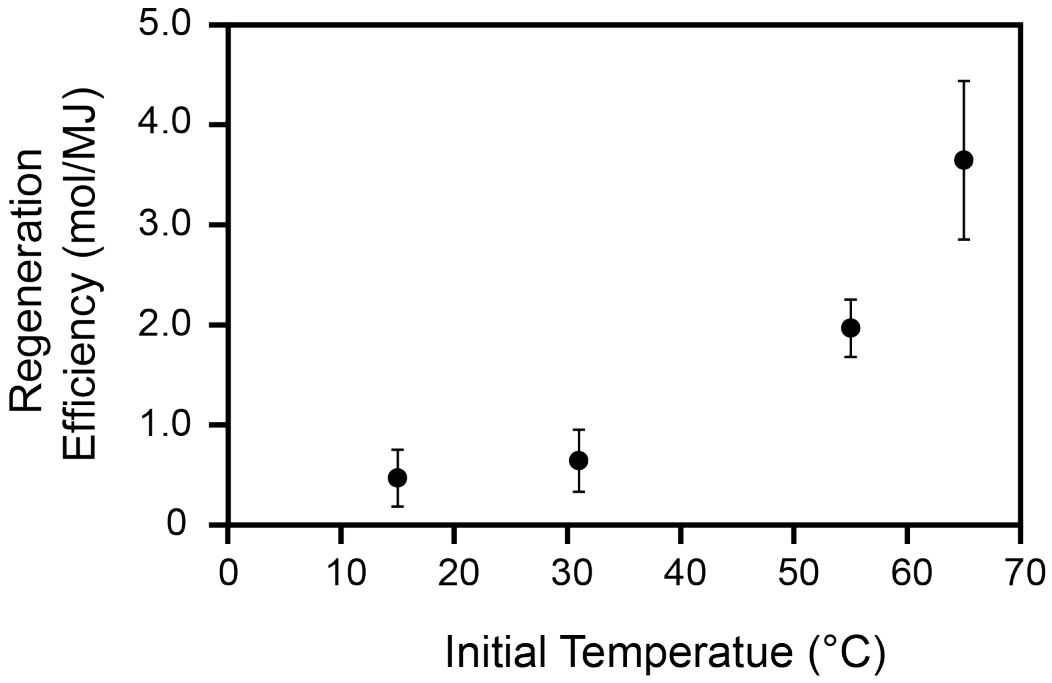

Figure 2.5: Initial temperature studies. As the initial temperature of the capture fluid increased, there was an increase in the regeneration efficiency. 0.1 wt% CB concentration was used. This figure is a reprint. [37]

We also explored the potential performance of solar energy for CO_2 stripping of a nanofluid, by estimating the surface area of incident solar light required to regenerate free MEA used in a 500 MW coal-fired power plant. In such a plant, on average, 2500 mol CO_2/sec are emitted. [40] With an average solar insolation of 561 W/m^2, an estimated 1.22 km^2 of surface area would be required to regenerate MEA, assuming 0.1 wt% CB and an initial temperature of 65 °C. [41] Our calculation assumes a flat surface as the interaction area between sunlight and the capture fluid. As a comparison, the Solar Energy Generating System in California [42] covers a total of 2.3 km^2 of field area, with the largest plant covering a field area of 0.48 km^2. Further optimization such as improved geometries, light collection, and thermal insulation could result in higher regeneration efficiencies and lower land usage. However, energy would still be required to pump the MEA and to compress the released CO_2 for storage. Detailed process conditions, simulations, and cost analysis are currently underway.

2.4 Experimental Details

2.4.1 Instrumentation

The solar simulator was custom designed and manufactured by Lee Moritz (University of California, Irvine Machine Shop). Desorbed CO_2 was measured for flow rate using a Cole-Parmer Gas Mass Flowmeter (32707-02), and for CO_2 concentration using a COZIR Wide-Range CO_2 Sensor that uses NDIR, fitted with Gold-plated optics (GC-0016). Hydrodynamic diameter measurements were recorded using a Malvern Zetasizer ZS Nano dynamic light

scattering instrument equipped with NIBS optics (ZEN 3600). Emission spectra of the light sources were examined using a Hitachi F4500 Fluorescent Spectrometer and a modified cuvette.

2.4.2 Nanoparticle Characterization

The CB nanoparticles were characterized with respect to their size and light absorbance. The nanoparticles were examined in water, 30 wt% aqueous MEA unsaturated and saturated with CO_2. The nanoparticles were distributed within the liquids at 0.001 wt% and dispersed under ultra-sonication. In water and MEA solution, the CB aggregate size ranged from 40 to 1000 nm, with an average of 200 nm (Figure 2.6). Upon CO_2 absorption, an increase in the size of CB aggregates was observed. It was inferred that when MEA is saturated with CO_2 and the nanofluid solution has a higher ionic strength (due to carbamates formed along with counter ions), CB nanoparticles have a resulting larger hydrodynamic radius. This phenomenon is explained by the DLVO theory, which states that the average hydrodynamic diameter should increase accordingly with increasing ionic strength. [43]

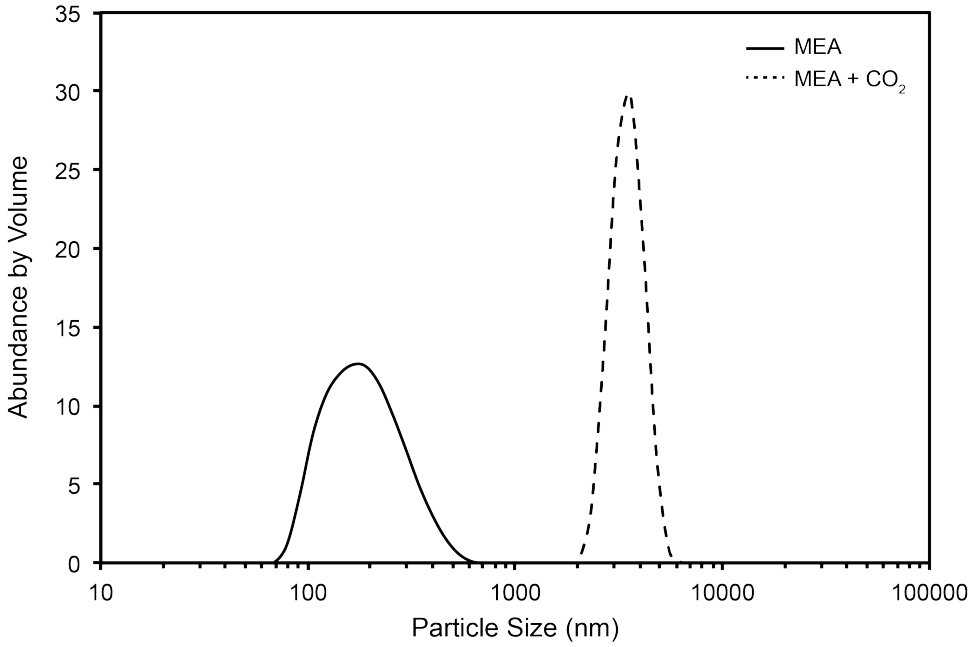

Figure 2.6: Nanoparticle size distribution on a logarithmic scale, comparison between capture nanofluid unsaturated and saturated with CO_2.

2.4.3 Light Source Emission Spectra

It should be noted that due to the IR absorbance of glass, only the spectra for the visible range ought to be considered.

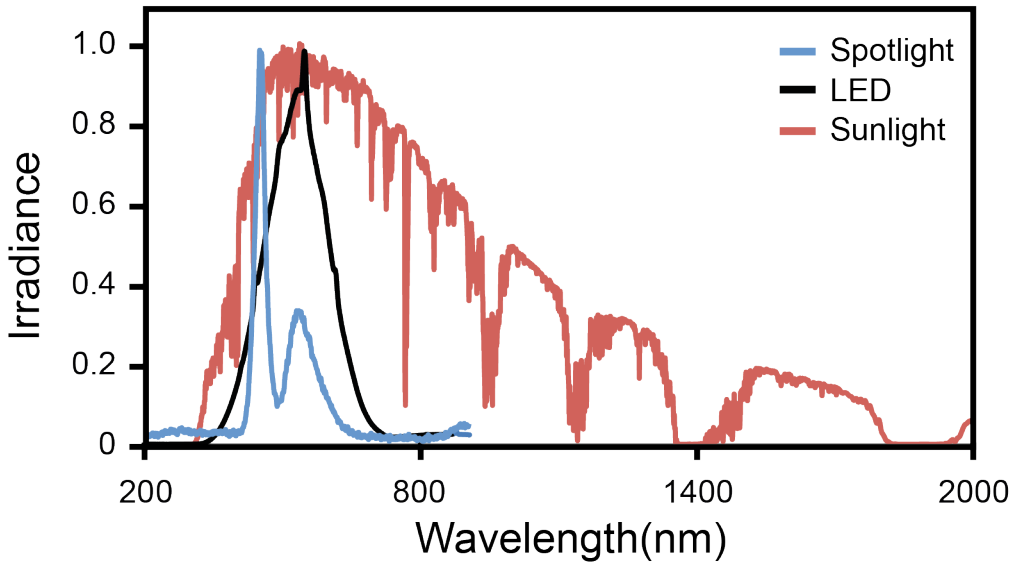

Figure 2.7: Light source emission spectra.

2.4.4 NMR Spectral Data

^{13}C NMR measurements were taken for the 30 wt% MEA CB nanofluid at three points: (a) before CO_2 absorption, (b) after CO_2 absorption, and (c) after CO_2 desorption.

(a) ^{13}C NMR (125 MHz, D_2O, 1,4-dioxane), δ = 67.19, 63.51, 43.10.

(b) ^{13}C NMR (125 MHz, D_2O, 1,4-dioxane), δ = 165.14, 161.51, 67.19, 62.05, 58.71, 44.03, 42.10.

(c) ^{13}C NMR (125 MHz, D_2O, 1,4-dioxane), δ = 164.97, 67.19, 63.01, 62.10, 44.11, 43.99, 43.18.

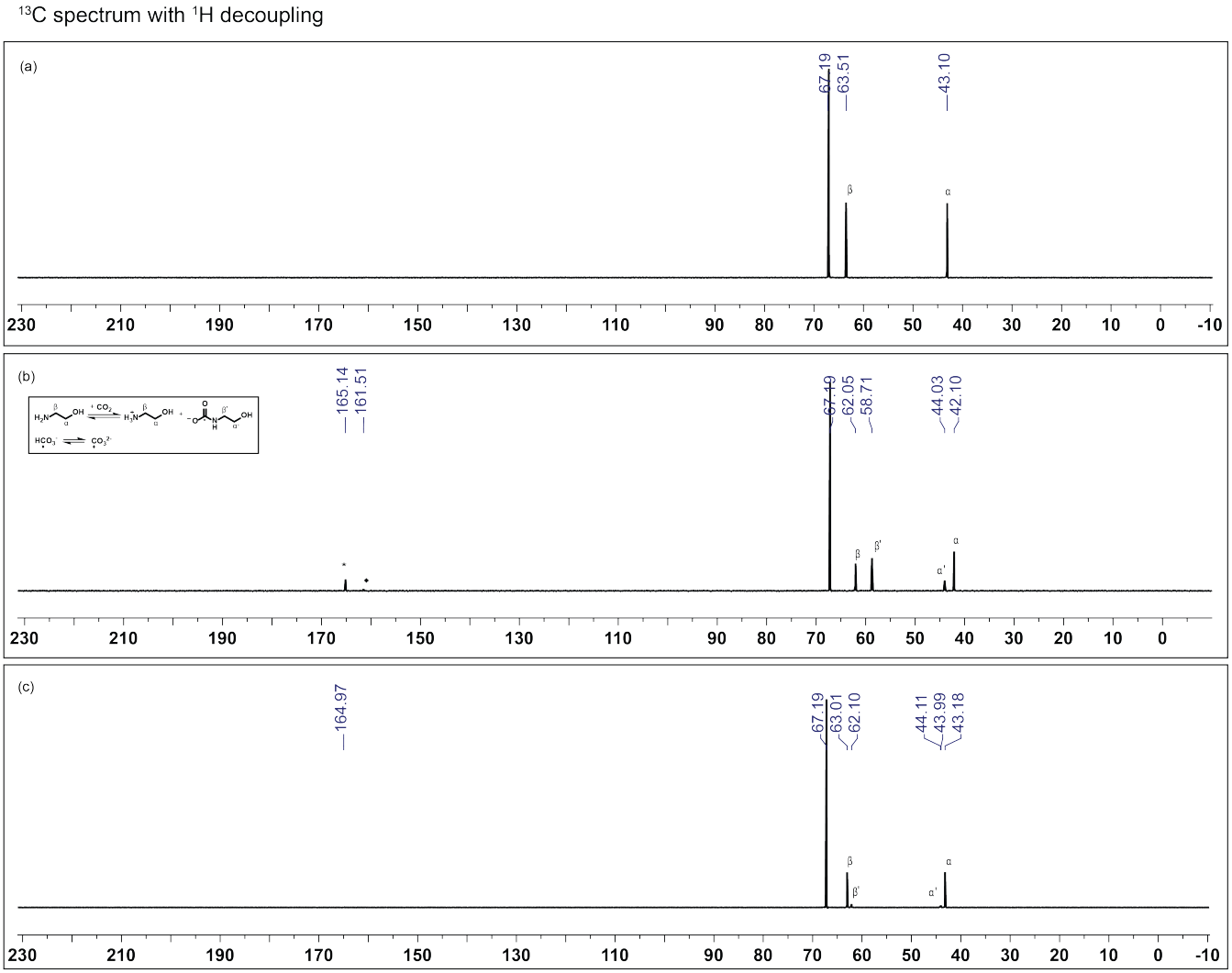

Figure 2.8: ^{13}C NMR of CB nanofluid **(a)** before CO_2 absorption, **(b)** after CO_2 absorption, and **(c)** after CO_2 desorption.

Chapter 3

Carbon Black Surface Modifications and Application

3.1 Introduction

Previously, we observed that oxidized nanoparticles enhanced photothermal regeneration of an aqueous MEA CO_2 capture fluid. This occurs when CB nanoparticles activated by light convert photo energy into thermal energy, resulting in breaking the C-N bond between CO_2 and MEA. These results show how a photothermal process might be used to drive chemical reactions in solution with increased energy efficiencies. The efficiency of a nanoparticle photothermal process in a liquid medium requires surface interactions between particle and solution, however these interactions are understudied.

We use CB to release CO_2 from capture solutions to lower the high cost and limitations of traditional methods for regenerating carbon capture solutions. CB has promising applications ranging from pharmaceutical drug-delivery vectors and bio-sensing devices to harvesting solar-energy, alongside use as conductive fillers in the rubber and electronic industries, such as fuel cells and lithium batteries. [44] In these applications, the highly irregular hydrophobic surface of nanopores is modified to influence acidity/basicity, wetting, and reactivity of CB. [45, 46, 47] CB

consists of aromatic sheets with disorganized nanopores, which may be represented schematically as an extreme case in Figure 3.1. [46, 46] As nature seeks to reduce surface energy, the highly irregular hydrophobic structure of CB, in addition to high surface area, often leads to the formation of aggregates of CB in solution. To prepare a stable CB-MEA nanofluid with enhanced CO_2 release efficiency, the CB surface was modified to achieve desired interactions between the CB nanoparticles and the solution.

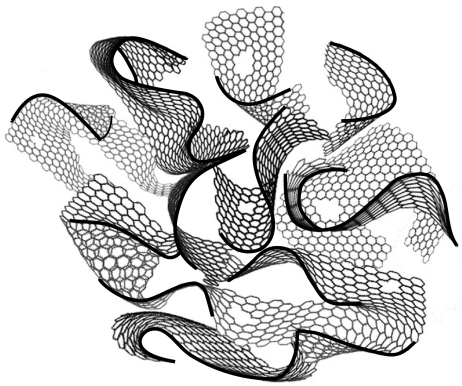

Figure 3.1: Proposed 3D structure of porous CB. The sp^2 graphene domains are highly irregular.

In this chapter, we highlight the effect of surface modification on photothermal efficiency of regenerating MEA by releasing CO_2. Modification of the CB surface changes the: (1) dispersability in solution, or aggregate size and (2) the amount of released CO_2 from chemically bound MEA. We modified the surface of CB particles to create surfaces composed of anionic sulfonates and neutral amines, both of which form stable nanofluids. The covalent surface

functionality was confirmed by X-ray photoelectron spectroscopy (XPS), Fourier-transform infrared spectroscopy (FTIR), thermogravimetric analysis (TGA), and Raman spectroscopy. Dispersion studies using dynamic light scattering (DLS) techniques showed that particle or aggregate size does not influence the photothermal effect.

To study the role of the covalent surface modification of CB, we probed how surface charge and chemical functionality of the nanoparticles change the amount of CO_2 released, providing initial mechanistic understanding of release. These surface functionalities on CB can improve or suppress the total amount of CO_2 released from MEA, indicating that surface properties influence the efficiency of chemical reactions activated by a photothermal effect. While the chemical release of CO_2 from MEA depends on the surface modification of the CB, the photothermal vaporization of water was not affected by the same modifications. This suggests that the surface modification does not affect the photothermal process, but rather enhances only the subsequent chemical reactions. Therefore, we conclude that the efficiency of decarboxylation in a heterogeneous solution is influenced by the surface functionality of a photothermal nanoparticle rather than an effect of physical dispersion or aggregate size.

3.2 Experimental

Reagents were purchased from Sigma-Aldrich and used as received without further purification unless otherwise noted. VULCAN® 9 N115 carbon black nanoparticles (CB-raw), donated from Cabot Corporation, were dried *in vacuo* at 90 °C for 48 hrs before use. Dichloromethane (DCM) was dispensed under argon from a glass solvent purification system custom manufactured by Jorg

Meyer (University of California, Irvine). Reagent grade carbon dioxide was purchased from Airgas.

3.2.1 Gas Desorption and Detection System for Capture Fluid Regeneration

In a modification to our initial experiments detailed in Chapter 2, all following experiments employ a reaction setup without the incoming air stream into the flask (Figure 3.2). The low CO_2 partial pressure of the air stream into the flask shifts the vapor equilibrium, biasing it towards more CO_2 release. By removing this parameter and only measuring the CO_2 output, more accurate measurements are made and there is greater reproducibility in between these static trials. Efficiency was calculated by mathematically combining the desorbed CO_2 percentage with the airflow rate, while considering input irradiance.

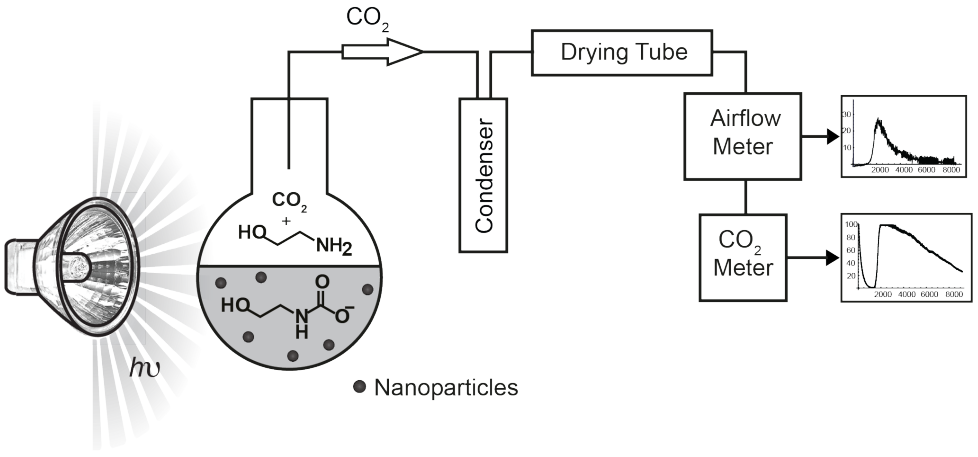

Figure 3.2: Schematic of photothermal regeneration. In a roundbottom flask filled aqueous MEA saturated with CO_2 and CB nanoparticles, a solarsimulator initiates the release of CO_2 which is analyzed by means of an airflow meter and CO_2 meter.

A 50 mL round bottom flask containing CB (40 mg, 0.1 wt%) and aqueous monoethanolamine (40 mL, 30% monoethanolamine in water (v/v)) respectively was sonicated for 20 mins, weighed, and gravimetrically saturated with 4 g of CO_2, 10 wt%. The following parameters were kept constant for all trials: (1) Halogen projector bulb light source, irradiance between 2800-3000 W/m^2 (~65 °C bulk heating), (2) 40 mL scale, and (3) stirring rate: 500 rpm.

3.3 Results and Discussion

3.3.1 Chemical Composition

Characterization of surface modification on CB is complicated due to the highly disordered surface; so multiple characterization techniques were employed to confirm covalent modification. Initially, the covalent modification of CB was confirmed by TGA and FTIR.

The presence of covalent functional groups on CB was analyzed by TGA and masses were recorded as a function of temperature. TGA curves show a mass loss corresponding to the covalent sodium sulfonation of the CB surface as shown in Figure 3.3. The loss of surface functional groups occurred in two stages: (1) the mass losses at 511 °C (9.6 wt loss %) and (2) the mass loss at 678 °C (6.2 wt loss %). Both are associated with the decomposition of $-SO_3Na$ from the CB surface. A control of the blank sample of mixed sulfanilic acid (SA) and CB-raw showed decomposition at a much lower temperature (250 °C) than the CB-SO_3Na.

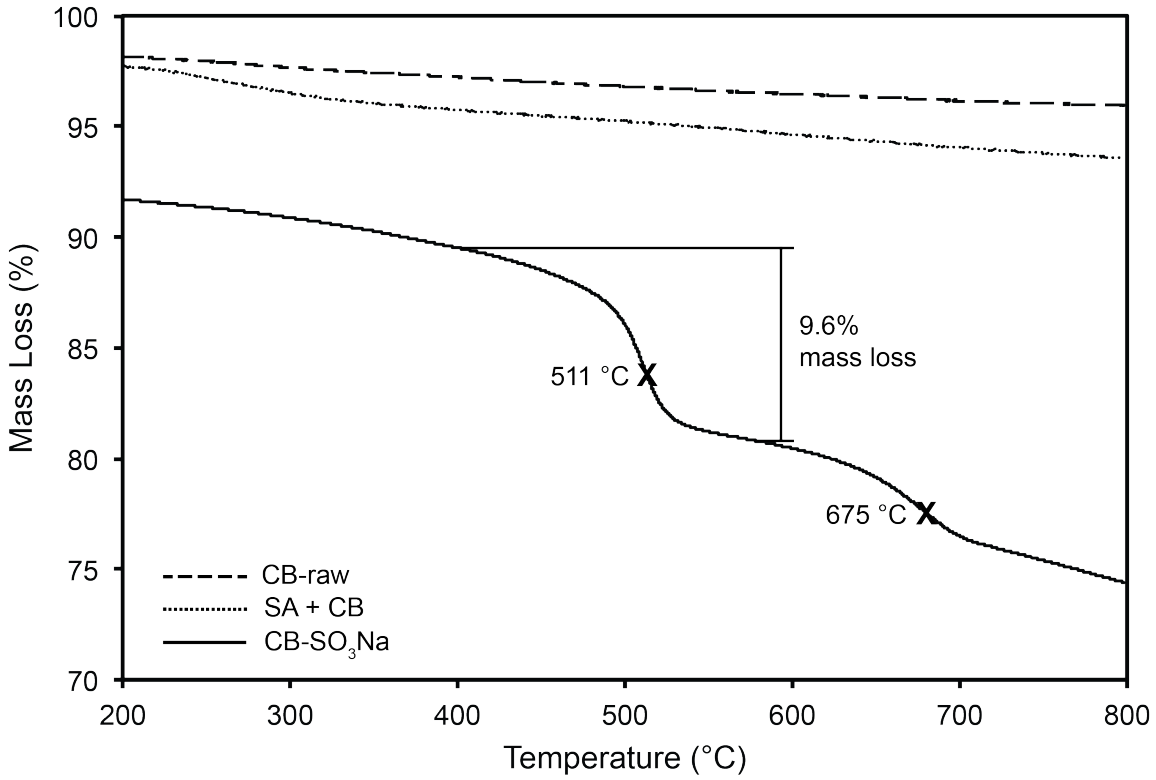

Figure 3.3: TGA curves for CB-raw, SA (sulfanilic acid) with CB control, and CB-SO_3Na. The loss of surface functional groups at 511 °C (9.6 wt loss %) and 675 °C (6.2 wt loss %) indicate covalent modification of CB with –SO_3Na.

In the trace of CB-SO_2-EDA, approximately 25% of mass was lost at 275 °C, which is attributed to the covalent sulfonamide attached to CB (Figure 3.4). The formation of covalent sulfonamide bonds to the surface of CB is apparent by comparison of the free ethylenediamine (EDA) decomposition, at a lower temperature of 70 °C to the EDA in CB-SO_2-EDA.

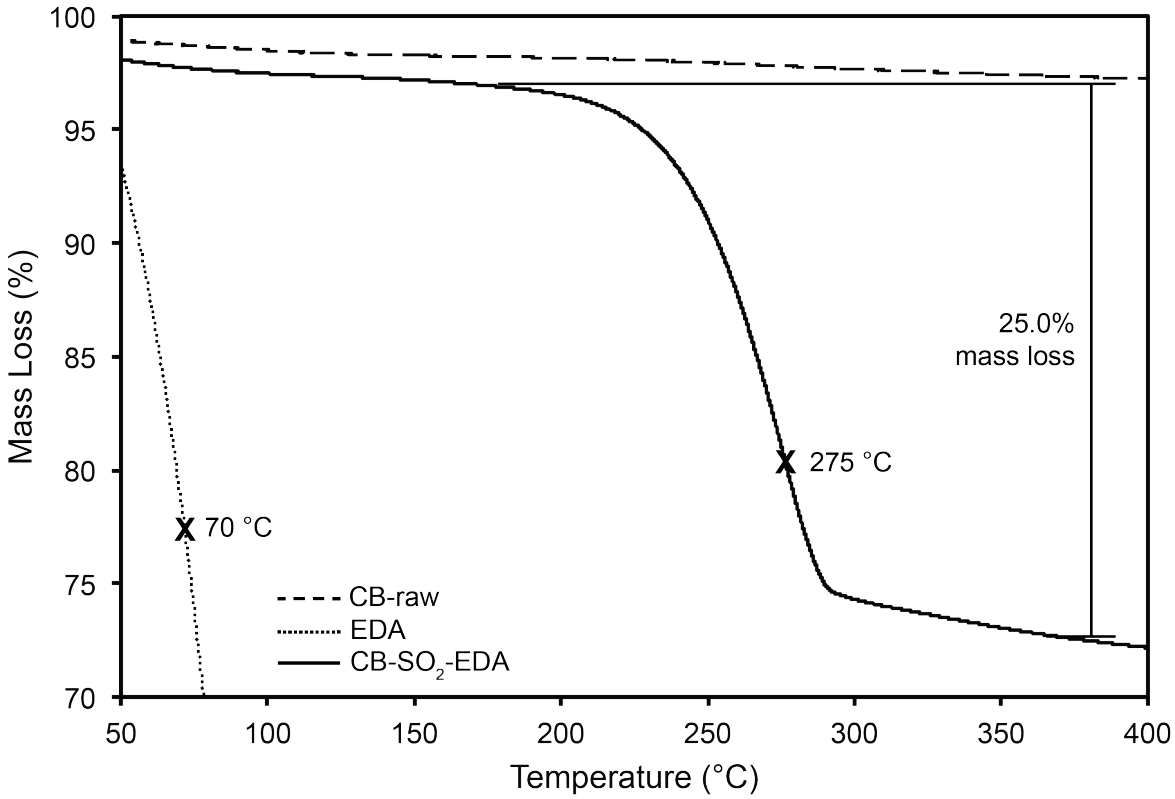

Figure 3.4: TGA curves for CB-raw, EDA (ethylenediamine), and CB-SO_2-EDA. The loss of surface functional groups at 275 °C (25.0 wt loss %) indicate covalent modification of CB from –SO_3Na to –SO_2EDA.

As shown in Figure 3.5, the FTIR spectra of CB-raw (unmodified) and modified CB-SO_3Na, and CB-SO_2-EDA differs significantly. The absorption bands were of weak intensity because of the black-body absorbing nature of carbon black. [48] However, normalized FTIR spectra provide useful relative information on surface modifications. A broad band centered at approximately 3450 cm^{-1} were observed in the spectra of all samples, and is likely due to O-H stretching of water absorbed in the KBr pellet. The band at 1630 cm^{-1} also observed in all spectra is attributed to C=C stretching of the CB. [49, 50]

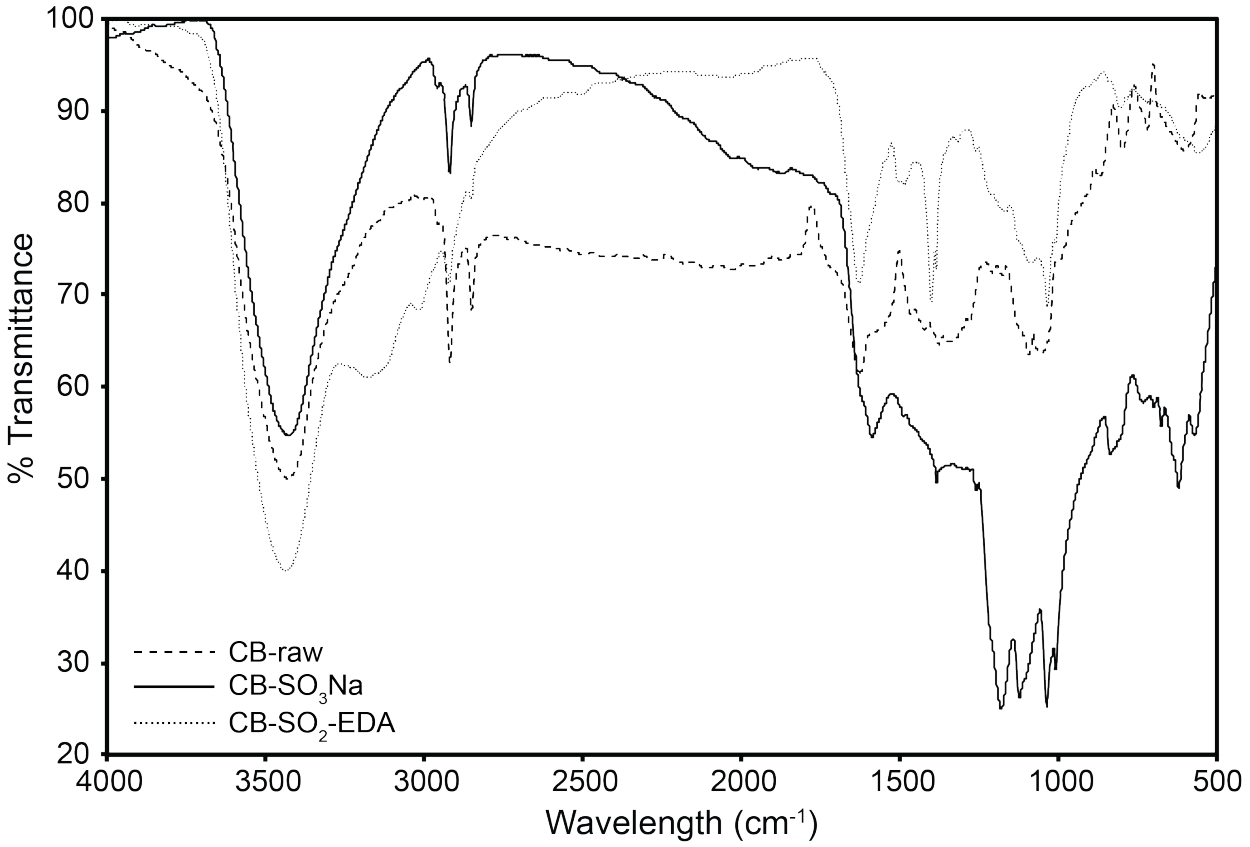

Figure 3.5: Overlapped FTIR spectra of CB-raw, CB-SO_3Na, and CB-SO_2-EDA. Differences in bands present in spectra of CB samples indicate successful covalent modification of CB with desired functionality.

As Figure 3.5 shows, after modification the FTIR spectrum of CB-raw differs significantly from that of CB-SO_3Na and CB-SO_2-EDA. Differences are also observed in the 1700–1000 cm^{-1} region and in the intensity of C-H bond stretching at 2919 and 2850 cm^{-1} attributable to C-H asymmetric and symmetric stretches, respectively. [48, 51, 52] Figure 3.5 also shows the difference in spectra of CB-SO_3Na and CB-SO2-EDA. Bands from approximately 1200-1100, and 620 cm^{-1} are attributed to the S=O stretch [53, 54] from the sulfonate in CB-SO_3Na and sulfonamide in CB-SO_2-EDA. Surface modification from the –SO_3Na to –SO_2-EDA induces a

slight loss of S=O bonds on the surface, as observed from the reduced spectral intensity of the peaks around 1200 cm^{-1}. There is also an increased spectral intensity of the peak at 3434 cm^{-1} in the CB-SO_2-EDA spectrum attributable to the N-H stretch. The new band appearing as a shoulder at 3180 cm^{-1} corresponds to N-H bond stretching. [55] The C-N stretching vibration is present at 1486 and 1034 cm^{-1} also appears in the CB-SO_2-EDA spectrum. [56] The bands present in both the spectra of sulfonate and sulfonamide surface modified CB along with the TGA data suggests that desired functionality was introduced onto the surface covalently, and was further confirmed with the following described techniques.

3.3.2 Chemical Structure

Raman spectroscopy was used to determine the degree of surface functionalization, as shown in Figure 3.20. Chemical structure and surface composition was independently confirmed with XPS analysis. Surface modification was confirmed by comparing high-resolution region XP spectra of elements respectively present in the unmodified and modified CB samples (Figure 3.6). The XPS survey scan for CB-raw is shown in Figure 3.12.

The C1s peaks of CB-raw displayed a main peak at 284.2 eV, which is attributed to the sp^2-hybridized carbon atoms present in the CB structure. [57] Figure 3.6 compares the wide-survey XP spectra for CB before and after CB-SO_3Na, and CB-SO_2-EDA functionalization.

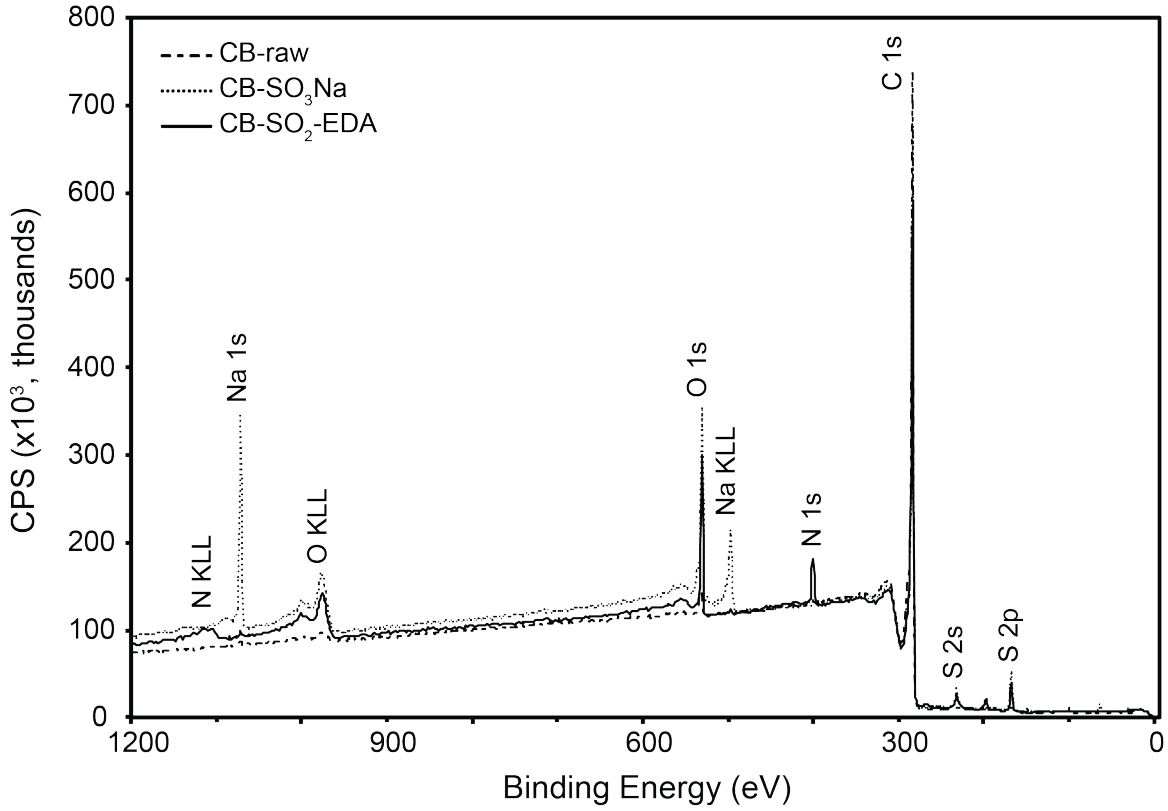

Figure 3.6: XPS wide-scan spectra of CB-raw, CB-SO_3Na, and CB-SO_2-EDA. Differences in elements present in spectra of CB samples confirm desired chemical surface functionality.

In a wide-survey scan for CB-SO_3Na, elements not present in the unmodified CB-raw appeared, such as S2p centered at 168.5 eV, and Na1s at 1072.1 eV. Similarly for the XP spectrum of CB-SO_2-EDA, elements not present in the unmodified CB-raw appeared, such as S2p centered at 168.5 eV, and N1s at 401.1 eV. Following the reaction with EDA, the Na1s peak is reduced indicating the conversion from $-SO_3Na$ to $-SO_2$-EDA. The modification on the surface of CB changes the chemical state of the respective elements. This change was monitored by the changes in the envelope shape of the high-resolution C1s, S2p, and N1s XP spectra recorded in the

modified nanoparticles. Deconvoluted high-resolution C1s, O1s, Na1s, S2p, and N1s XP spectra for these carbon samples are shown in Figure 3.13 – Figure 3.19.

In the case of CB-SO_3Na, the deconvoluted S2p spectrum confirms the formation of sulfonic acid and oxidized sulfur species (Figure 3.17). In the case of CB-SO_2-EDA, the deconvoluted N1s spectrum confirms the formation of amine and amide groups on the CB-SO_2-EDA surface (Figure 3.19).

3.3.3 Carbon capture regeneration efficiency

After confirming that the surface of CB was covalently modified with the desired surface functionality, we assessed the application of the modified particles as nanofluids by measuring the efficiency of a decarboxylation reaction (and subsequent CO_2 solvent regeneration) due to photothermal heating. To measure the release of CO_2 using the photothermal effect, we used our previously developed gas desorption and detection system to characterize the regeneration of CO_2 capture fluids. [37] All reactions were run as 0.1 wt% CB nanofluids in 30 wt% MEA with 2945 W/m^2 input light irradiance resulting in a low bulk temperature of ~65 °C. A plot of total mass of CO_2 released for each modified CB nanofluid is shown in Figure 3.7. With the inclusion of an amine on the surface, CB-SO_2-EDA released the highest amount of CO_2, ~70% more CO_2 than the unmodified CB-raw. While in contrast, CB-SO_3Na released the lowest amount of CO_2, ~60% less than the unmodified CB.

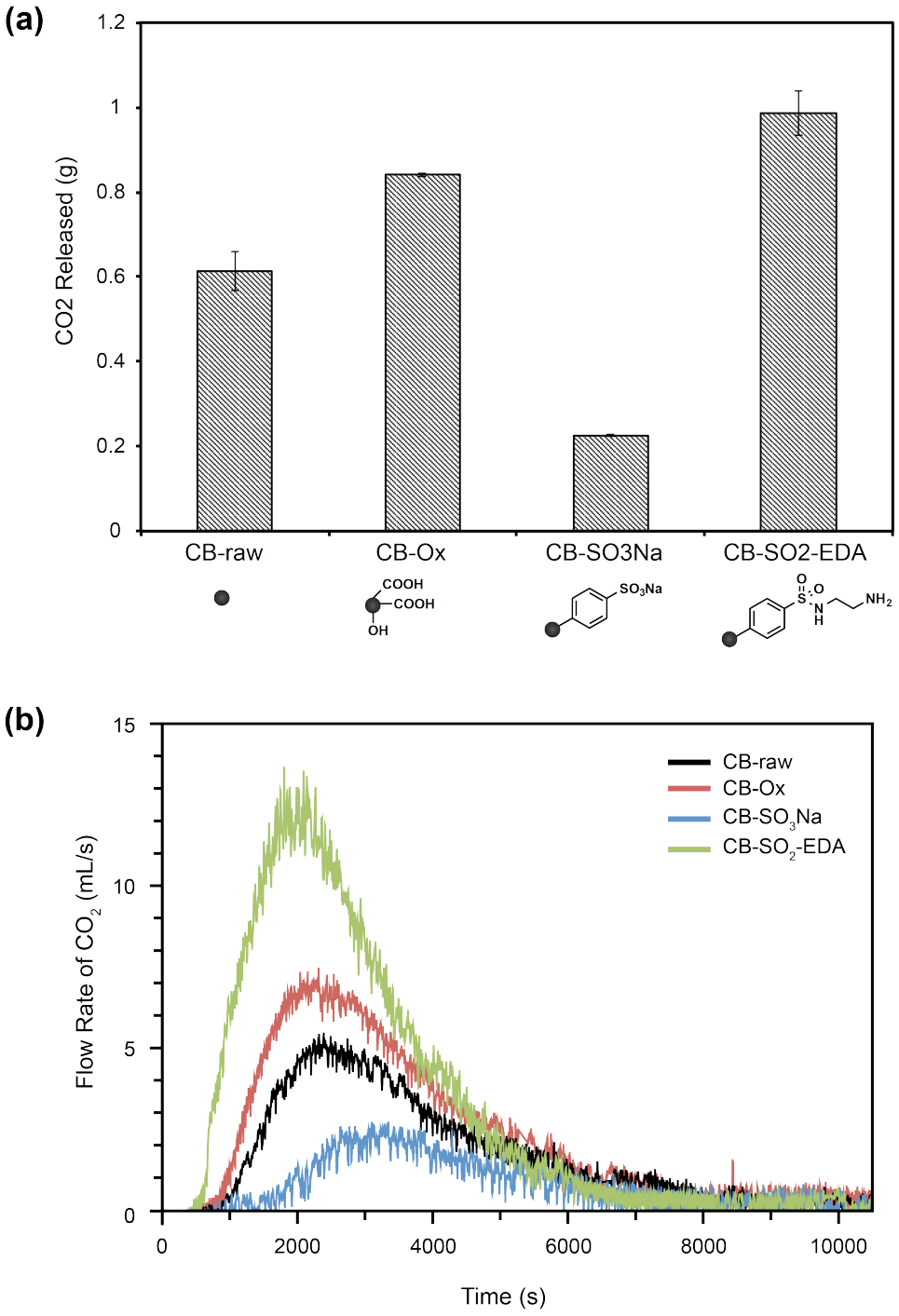

Figure 3.7: Effect of surface modification on CO_2 decarboxylation. Solvent regeneration, assessed as CO_2 release, varies from CB samples signifying an effect of surface functionality. (**a**) Total grams of CO_2 release for each CB nanoparticle sample as calculated from raw flow data. (**b**) Raw flow data for CB samples.

It was necessary to determine if the increased and decreased rates of CO_2 release were related to the chemical process of decarboxylation, wherein the surface functionality affected the release, or if the modification changed the efficiency of the photothermal process by altering aggregate sizes of the particles. To test if the change seen in photothermal CO_2 release profiles was a result of the chemical reactivity of modified CB-raw, and not aggregate size, DLS was employed to monitor how surface functionality affects aggregate sizes. Simultaneously, we conducted experiments analogous to the work of Halas [17], where a photothermally active nanoparticle in water produced steam when stimulated with light. If the nanofluids had similar dispersivity (measured as aggregates sizes), or produced the same amount of steam, then the result was not a physical effect of the surface modification.

CB nanofluids were formulated in double distilled water in an identical manner to the CO_2/MEA experiments above. Figure 3.8a compares mass loss of CB samples in 30 wt% aqueous MEA saturated with and without CO_2. This experiment allowed us to conclude whether the surface modification affects the physical photothermal process of steam generation, or the chemical reaction and solvent regeneration by decarboxylation. Figure 3.8b compares mass loss of CB samples in 30 wt% aqueous MEA without CO_2 and in water. In nanofluids without CO_2, the photothermal energy conversion drives a phase change to produce steam rather than the chemical decarboxylation reaction of CO_2. This experiment determined if the mass loss in 30 wt% aqueous MEA differed from the mass loss due to steam (in the 100% water nanofluids) indicating that aggregate size would change the photothermal effect.

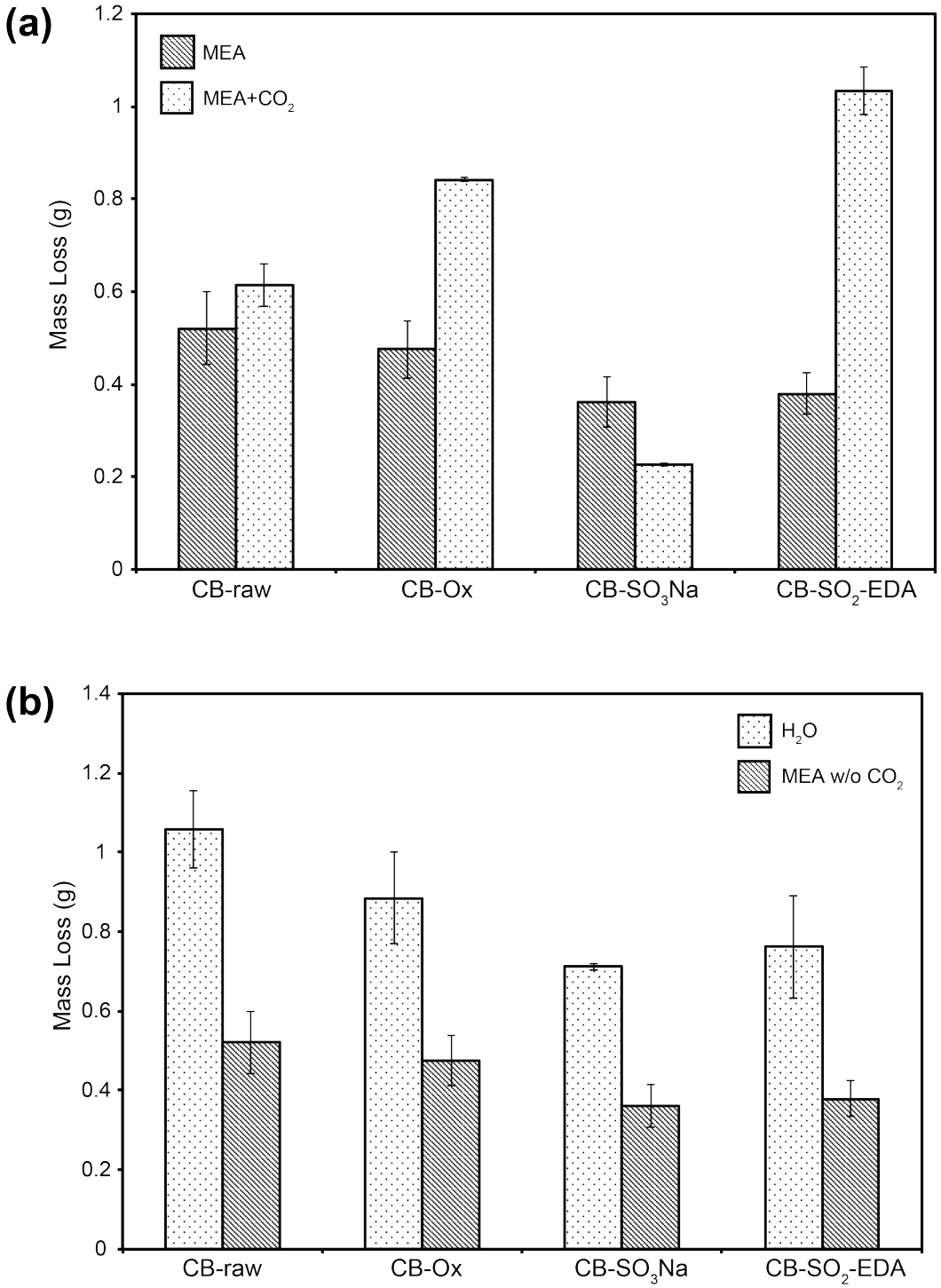

Figure 3.8: Mass loss as a result of CB surface functionality. **(a)** CB samples are prepared as nanofluids in 30 wt% aqueous MEA, saturated with and without CO_2. **(b)** CB samples are prepared as nanofluids in H_2O and unsaturated 30 wt% aqueous MEA.

A difference in mass loss due to surface functionalization is presented in Figure 3.8. There is no similar trend between CB samples in 30 wt% aqueous MEA, saturated with and without CO_2. We conclude from this data that the differences in mass loss due to vaporization and CO_2 release should be considered independent from each other. The surface modification affects the chemical process, CO_2 release via decarboxylation, rather than the physical steam generation caused by altered aggregate sizes of the particles. Figure 3.8 also shows the similarity between nanofluids of mass loss of CB samples in unsaturated aqueous MEA. A comparable trend exists in 100% water CB samples. There is no increased mass loss due to surface functionality, as seen in CO_2 saturated 30 wt% aqueous MEA.

To clarify that the nanofluid dispersity and nanoparticle aggregate size were not responsible for increased CO_2 release, we compared mass loss to hydrodynamic radii between the chemical and physical effects of the release of CO_2 (Figure 3.9).

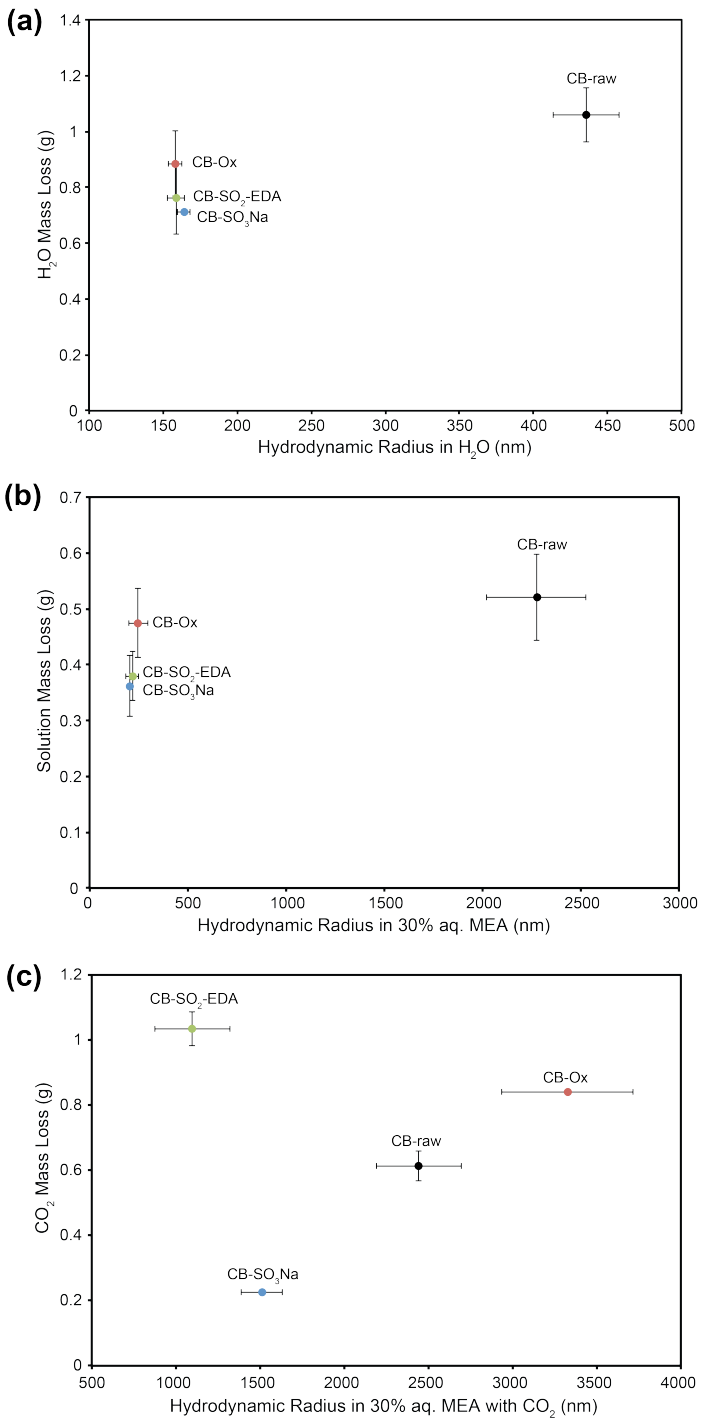

Figure 3.9: Mass loss as a result of nanofluid dispersitivity. (**a**) CB samples are prepared as nanofluids in H_2O, mass loss as a result of steam generation. (**b**) CB samples are prepared as nanofluids in unsaturated aqueous MEA, without CO_2. (**c**) CB samples are prepared as nanofluids in aqueous MEA saturated with CO_2, mass loss due to decarboxylation.

Although surface modification does change aggregate sizes in both H_2O and aqueous MEA, there is no trend indicating that aggregate size influences steam generation or CO_2 release. There is also no similarity in efficiency of steam generation and CO_2 release between surface functionality. Therefore, surface functionality does not affect the photothermal process itself; and we conclude it must change the rate of reaction in CO_2 release, analogous to how a change in ligand functionality can change the reactivity of a catalyst.

3.4 Experimental Details

3.4.1 General Procedures and Instrumentation

FTIR spectra were obtained with a Perkin-Elmer Frontier spectrometer (L1280034) under ambient conditions. Test samples were prepared by uniformly dispersing the CB in KBr and compressing the powder into pellets. The spectra were obtained in the wavenumber range 4000–600 cm^{-1}, typically 64 scans at a resolution of 4 cm^{-1} were accumulated for each spectrum. TGA measurements were performed on a TA Instruments TGA Q5000 thermogravimetric analyzer. The samples were analyzed at a heating rate of 10 °C min^{-1} from 30 to 800 °C under an atmosphere of inert air flowing at 40 mL min^{-1}. X-ray photoelectron spectroscopy was performed using an Axis-Supra analyzer (Kratos Analytical Ltd., Manchester, UK) equipped with a monochromatic Al X-ray source. The pressure of the analysis chamber during acquisition was lower than $5x10^{-9}$ torr. The X-ray spot size used for these experiments was 300 x 800 μm^2. Survey spectra used to determine surface elemental composition were recorded with a pass

energy of 160 eV, in the binding energy range from 0–1200 eV in 0.5 eV steps. At least two spots on one or more replicates were analyzed for each sample type. Photoelectron lines were recorded. The high resolution of the main constituent elements, i.e., O1s, N1s and C1s, spectra were acquired at an analyzer pass energy of 20 eV in 0.01 eV steps with a 300 ms dwell time. Quantitative analysis, based on peak area intensities after removal of the Shirley-type background, was performed by CasaXPS using the Kratos elemental library. Hydrodynamic diameter measurements were recorded using a Malvern Zetasizer ZS Nano dynamic light scattering instrument equipped with NIBS optics (ZEN 3600). Raman spectra were recorded with all analyses collected at a single point on the CB samples, performed using lens with 50x and 532 nm laser with a low laser power to avoid any heating effect using a Renishaw inVivo Raman microscope (H14087). The solar simulator was custom designed and manufactured by Lee Moritz (University of California, Irvine Machine Shop). Desorbed CO_2 was measured for flow rate using a Cole-Parmer Gas Mass Flowmeter (32707-02), and for CO_2 concentration using a COZIR Wide-Range CO_2 Sensor that uses NDIR, fitted with Gold-plated optics (GC-0016).

3.4.2 Experimental Procedures and Characterization Data

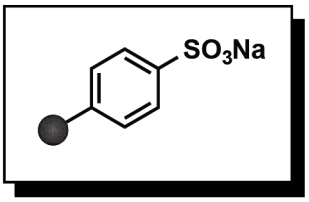

CB-SO_3Na. Carbon black was covalently modified using 4-aminobenzenesulfonic acid and sodium nitrite. The introduction of anionic groups (-SO_3Na) onto the surface of CB nanoparticles was achieved via generation of a diazonium salt in situ. [58] 0.5 g of CB, and 5.0 g of 4-aminobenzenesulfonic (sulfanilic) acid in 6 mL of H_2O were heated to 80 °C while stirring under normal atmospheric conditions for 10 mins where 2.0 g of sodium nitrite (dissolved

in 1 mL H_2O) was added drop wise. After 6 hrs of stirring and heating at 85 °C, the reaction was cooled to RT, and diluted with H_2O where the insoluble black material was then centrifuged and rinsed thoroughly twice with H_2O (20 mL). The desired product was isolated by evaporation of water under vacuum at 80 °C for 24 hrs.

In order to clarify the nature of the -SO_3Na attachment onto CB-raw, a control experiment was made using a sample of the reaction described above without sodium nitrite. A mixture of 100 mg of crude CB, 1.0 g sulfanilic acid (SA) and 1 mL H_2O was heated to 80 °C in an oil bath and maintained at this temperature for 6 hrs. The insoluble black material was then centrifuged and rinsed with H_2O. This material referred to hereafter as a blank sample was dried in an oven at 85 °C for 24 hrs.

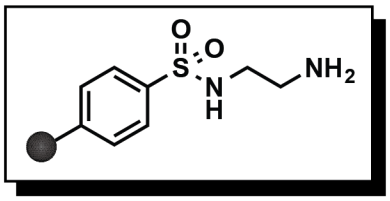

CB-SO_2-EDA. Carbon black was covalently modified by transforming the sulfonyl chloride into a series of sulfonamides. The introduction of amine groups (-EDA) onto the surface of CB nanoparticles was achieved by first activating the sulfonate with thionyl chloride, and then adding ethylene diamine. [59] 0.25g of CB-SO_3Na in 15 mL of dichloromethane (DCM) was sonicated for 20 mins in a round bottom flask where it was sparged with argon gas, and cooled to 0 °C. Under constant stirring, 3 mL of thionyl chloride was added to the black suspension and the reaction mixture was warmed to RT and maintained at this temperature for 3 hrs. Excess thionyl chloride was removed under rotary evaporation, whereupon 0.25 g of CB-SO_2Cl was resuspended in 7 mL of DCM. The reaction mixture was sonicated for 20 mins, sparged with argon, and cooled to 0 °C. Under constant stirring, 3.0 mL of ethylenediamine was added to the black suspension. The reaction mixture was

warmed to RT and allowed to stir for 8 hrs. A black solid was collected by Buchner filtration, washed with 1 M hydrochloric acid (20 mL), and water (20 mL), and dried under vacuum at 80 °C for 24 hrs to yield CB-SO_2-EDA as a black crystalline powder.

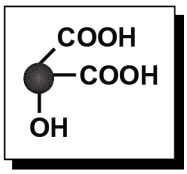

CB-Ox. CB-raw was oxidized according to the method described by Li et al. [60] 20 mL of a 2 M solution of ammonium persulfate (9.1 g) in 1 M HCl was added to a 1.0 g mass of dried CB, then the reaction was heated to 55 °C and maintained for 6 hrs. The CB-Ox was subsequently washed with water until a neutral pH was established. The material was isolated via centrifugation, and dried at 80 °C for 24 hrs.

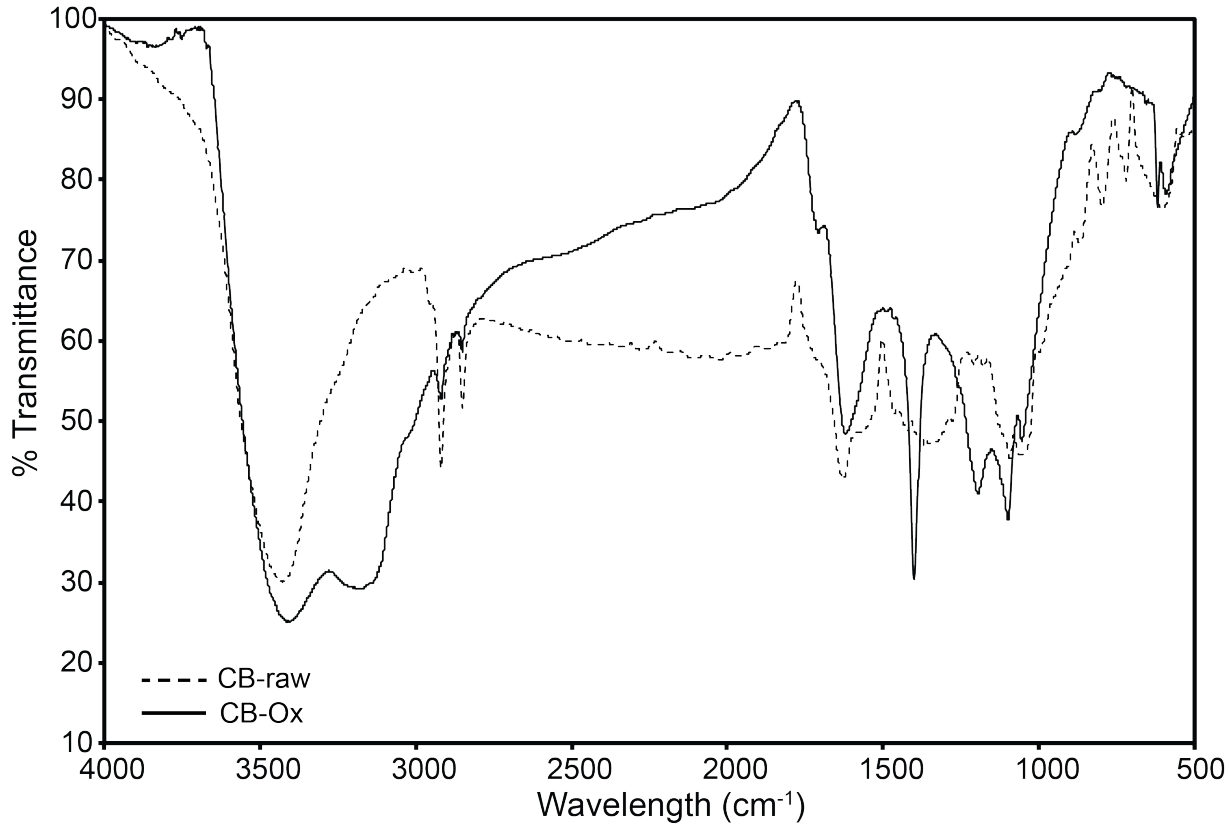

Figure 3.10: FTIR analysis of CB-Ox.

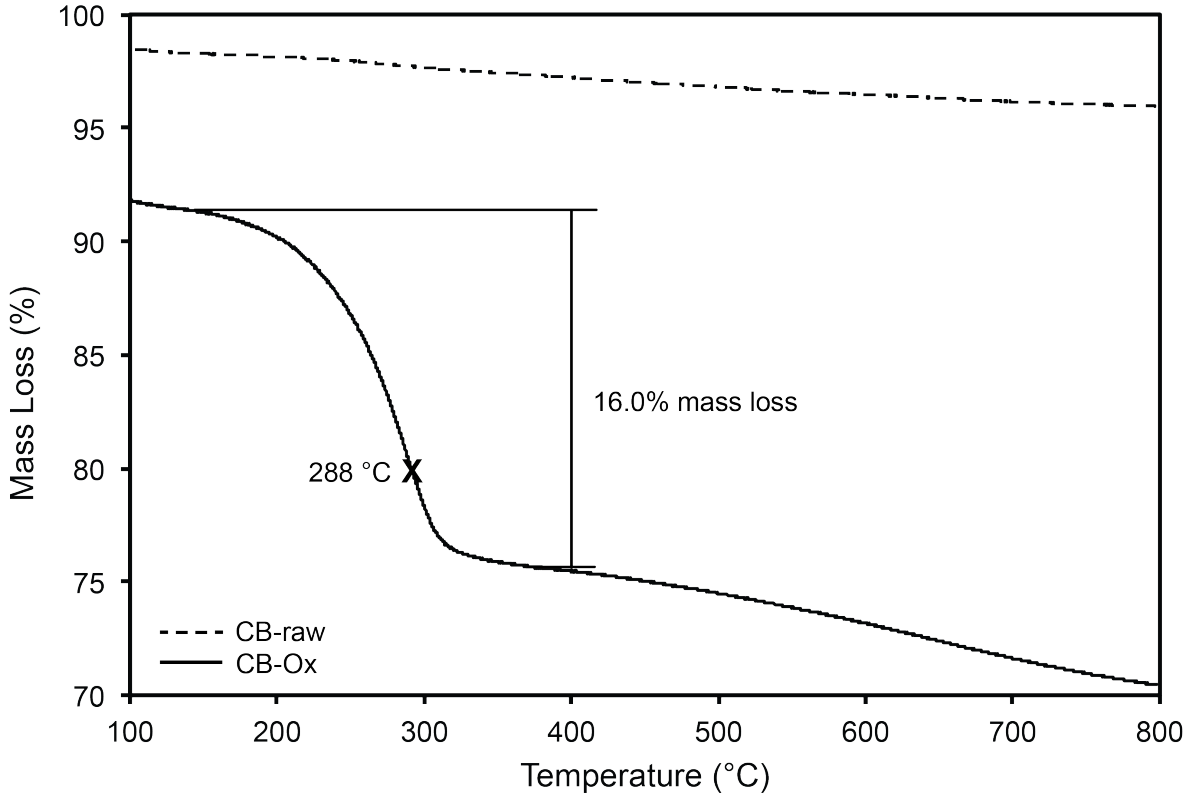

Figure 3.11: TGA analysis of CB-Ox.

3.4.3 XPS Spectral Data

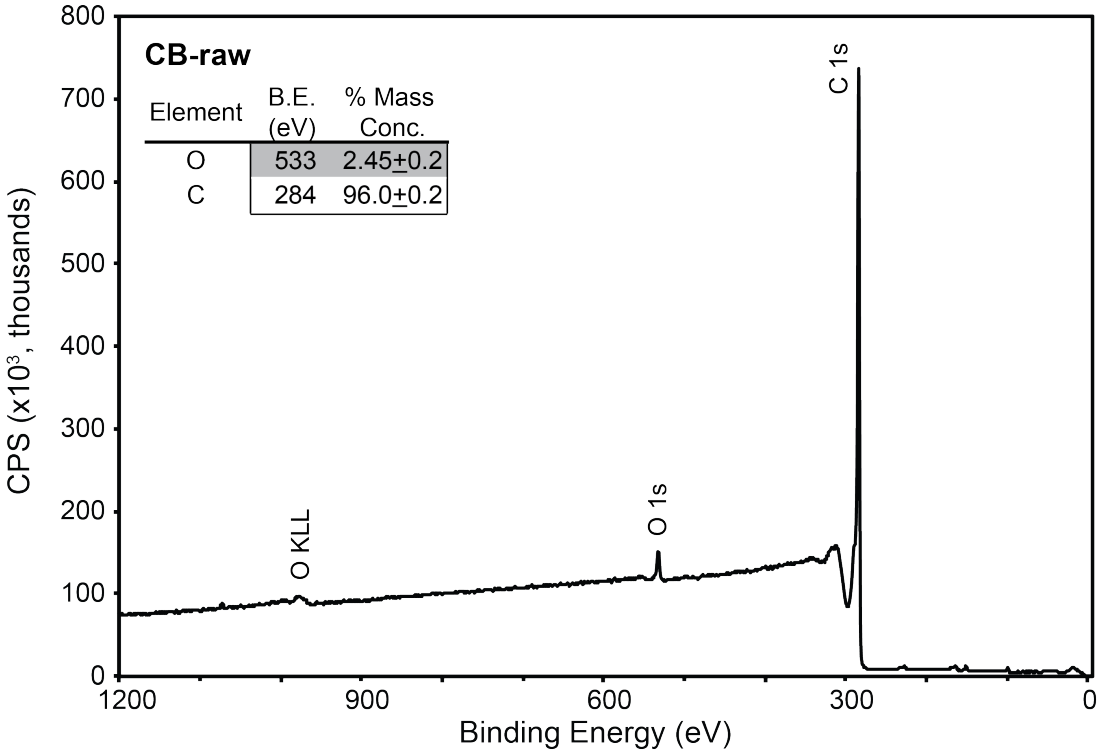

Figure 3.12: Wide-survey XP spectrum for unmodified CB-raw.

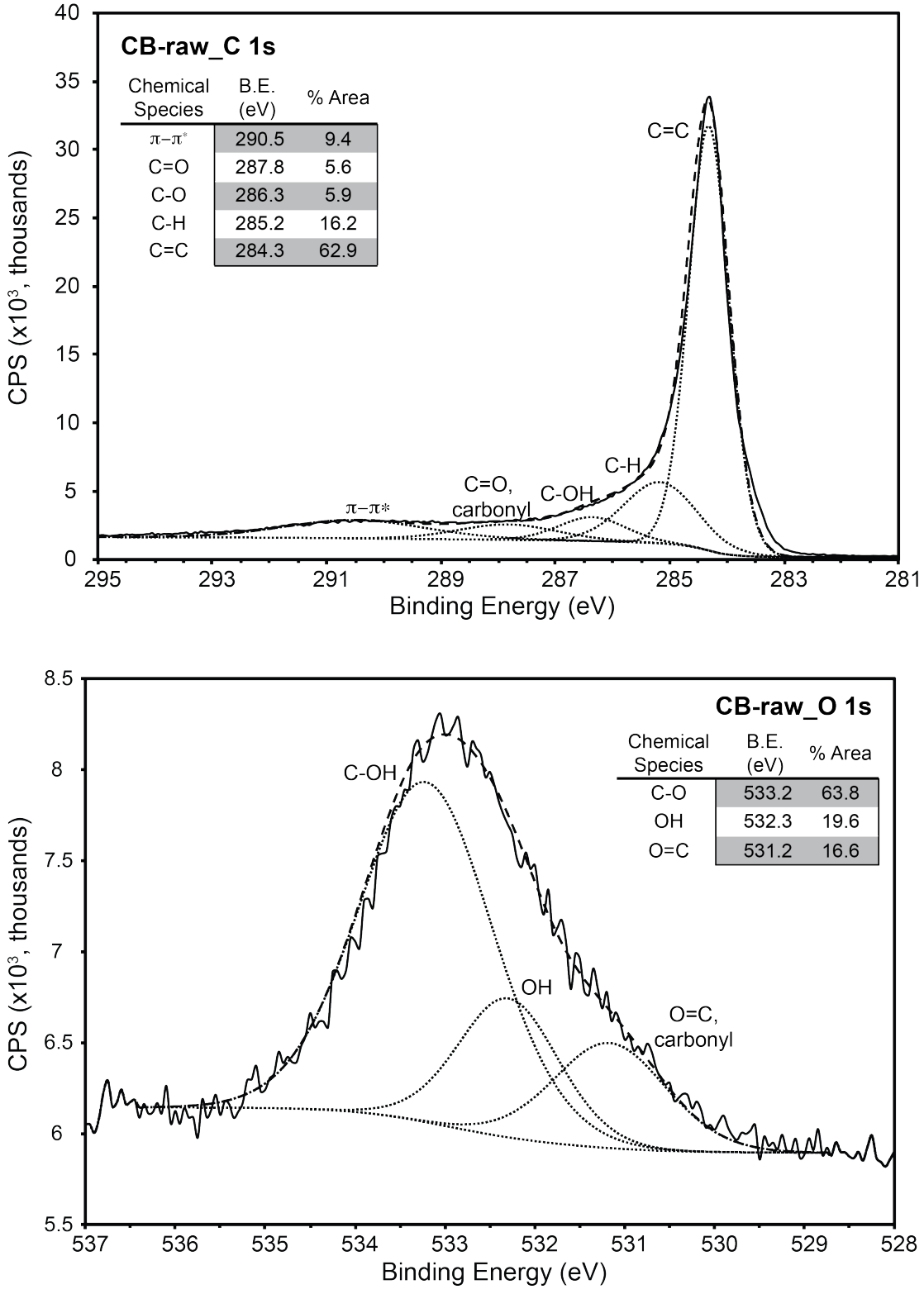

Figure 3.13: High-resolution C1s, and O1s XP spectra of unmodified CB-raw.

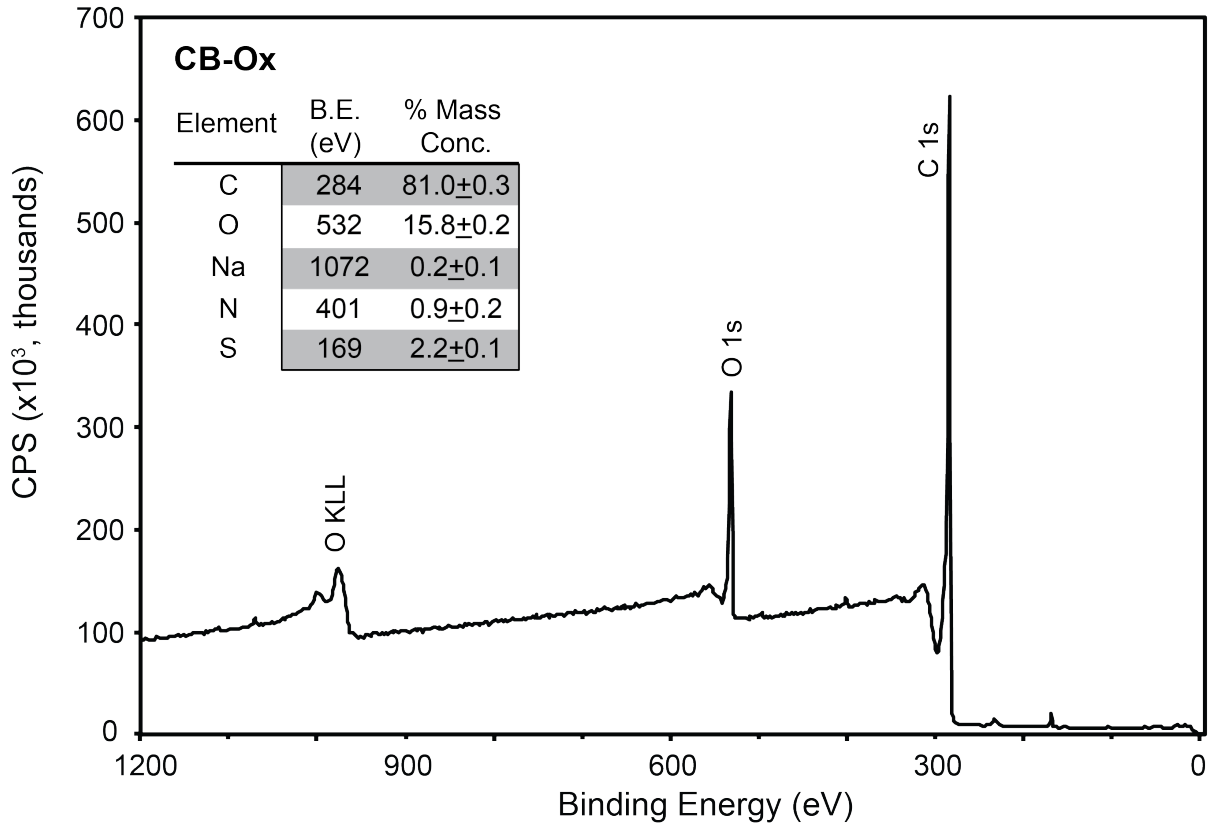

Figure 3.14: Wide-survey XP spectrum for CB-Ox.

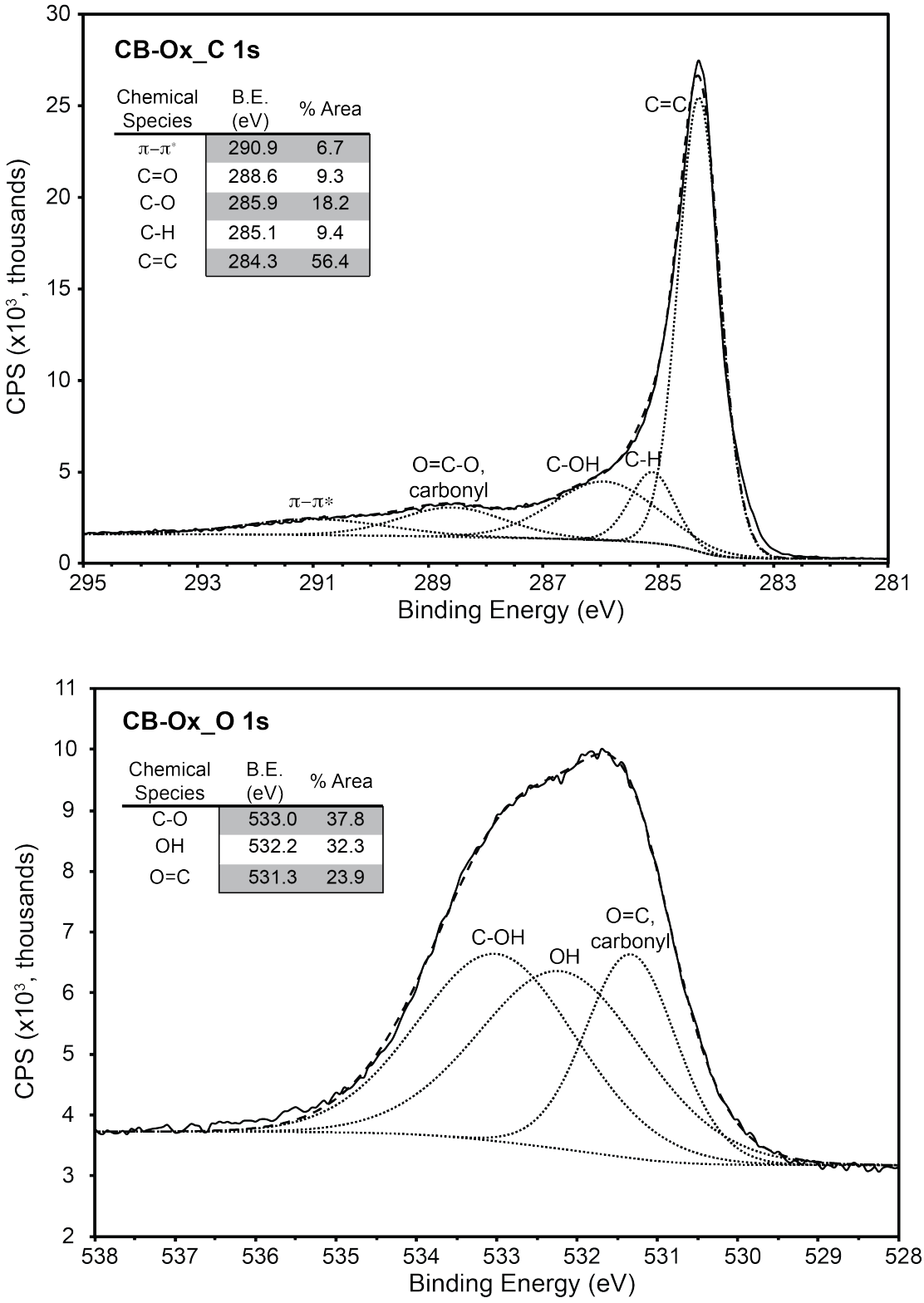

Figure 3.15: High-resolution C1s, O1s XP spectra of CB-Ox.

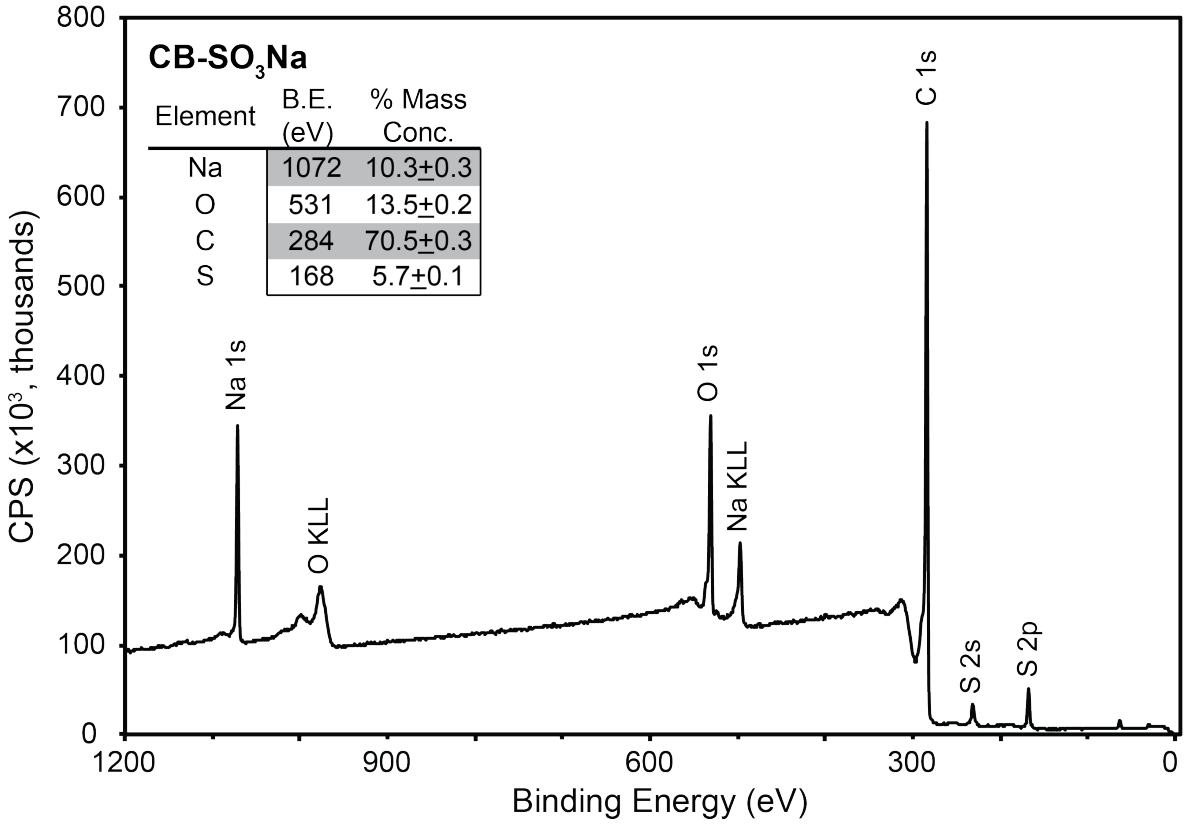

Figure 3.16: Wide-survey XP spectrum for CB-SO_3Na.

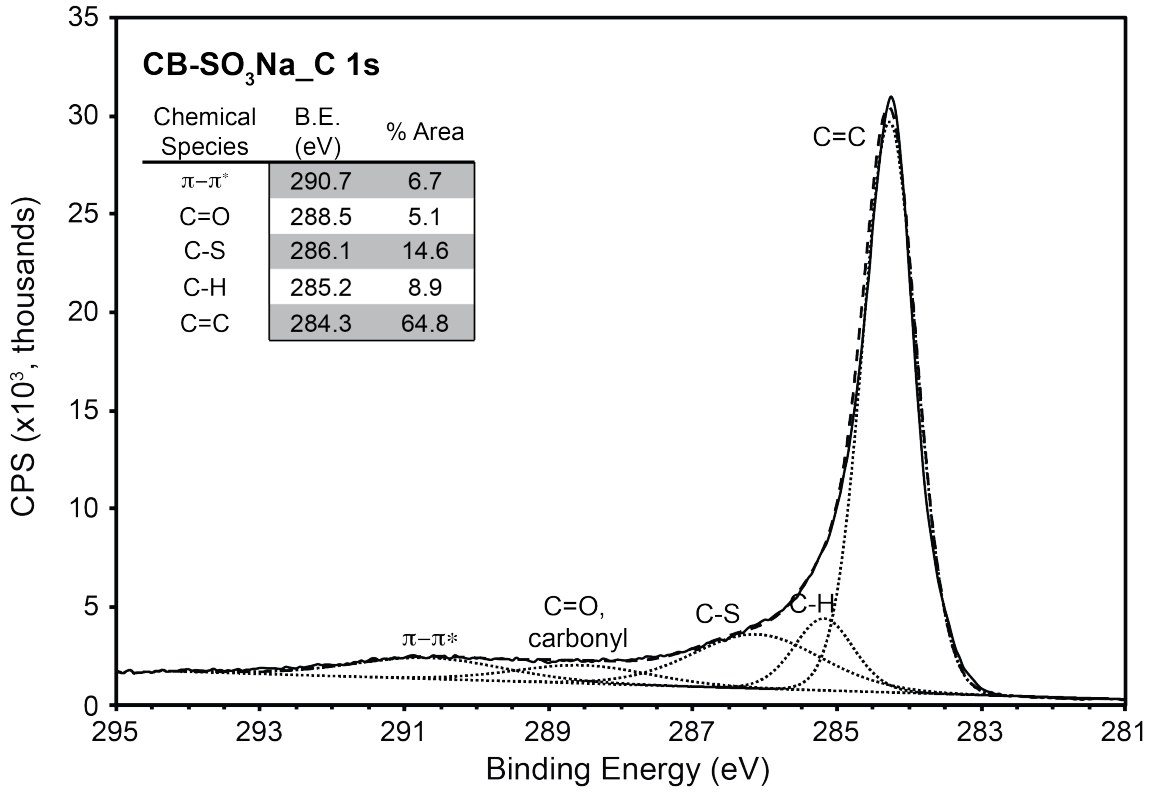
CB-SO3Na_C 1s
Chemical Species
B.E. (eV)
% Area
π–π*
290.7
6.7
C=O
288.5
5.1
C-S
286.1
14.6
C-H
285.2
8.9
C=C
284.3
64.8
C=C
C-H
C-S
C=O, carbonyl
π–π*
CPS (x10³, thousands)
Binding Energy (eV)

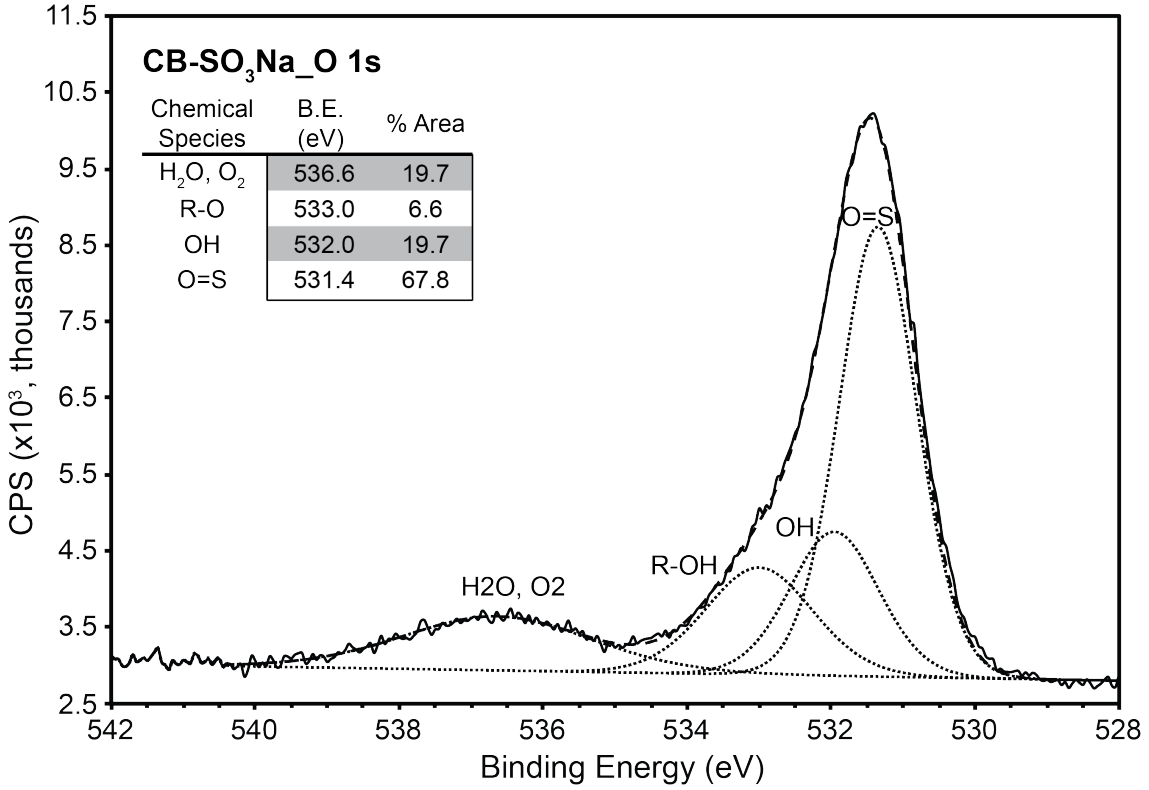
CB-SO3Na_O 1s
Chemical Species
B.E. (eV)
% Area
H2O, O2
536.6
19.7
R-O
533.0
6.6
OH
532.0
19.7
O=S
531.4
67.8
O=S
OH
R-OH
H2O, O2
CPS (x10³, thousands)
Binding Energy (eV)

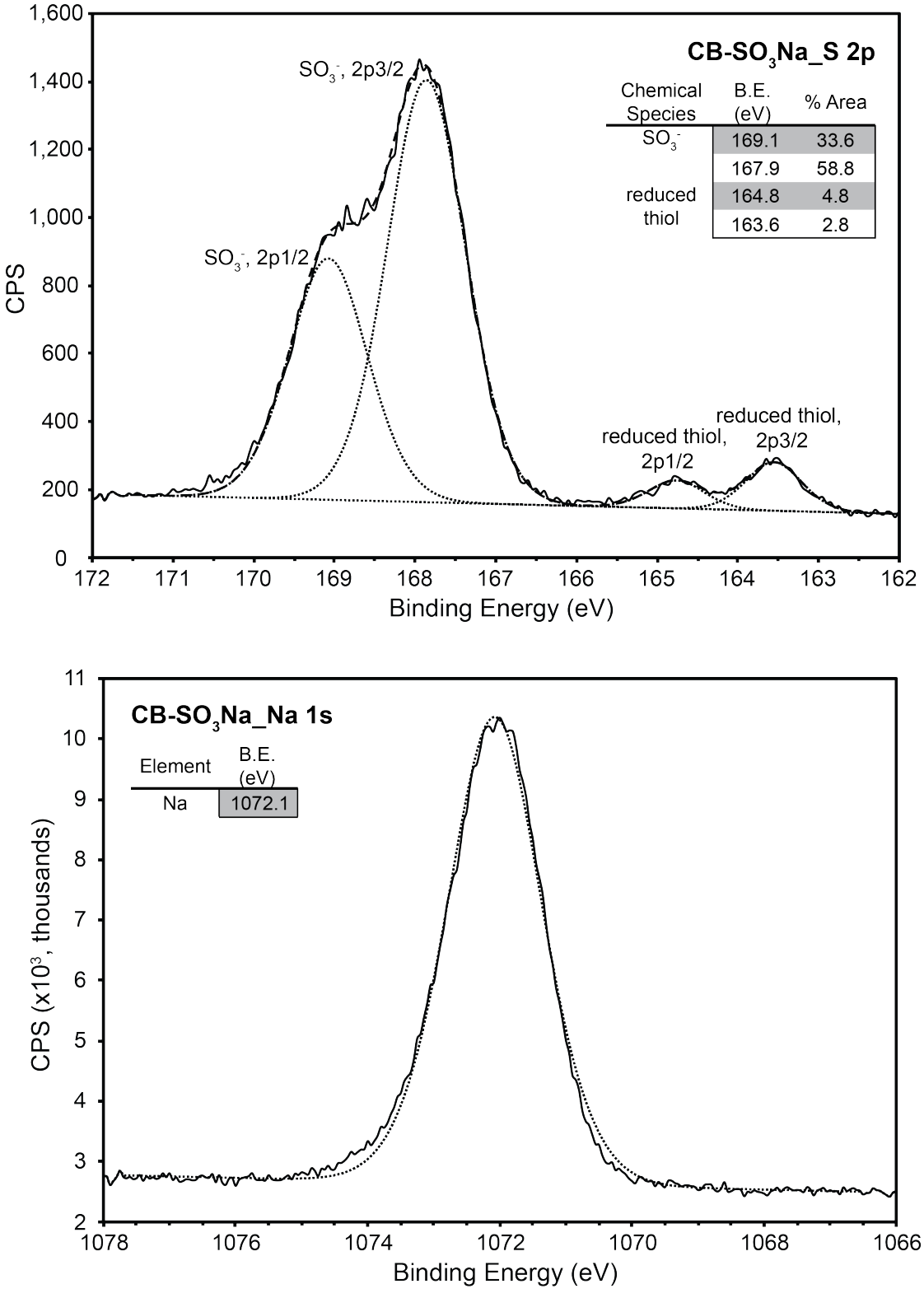

Figure 3.17: High-resolution C1s, O1s, S2p, and Na1s XP spectra of CB-SO_3Na.

In the case of CB-SO_3Na, the S2p high-resolution XP spectrum was deconvoluted into two doublets with peaks located at 167.9 and 169.1 eV, assigned to the sulfonic acid groups associated with sodium (-SO_3Na). [61] This doublet centered at 168.5 eV is attributed to the oxidized sulfur species while the second doublet centered at 164.2 eV is due to a reduced thiol species [62]. The high-resolution O1s XP spectrum shows an increase in the peak at 531.4 eV assigned to species with an oxygen double bond. Its peak intensity increase is explained by the contribution of S=O bonds incorporated onto the CB surface. [63] The peaks located at 531.4 and 533.0 eV correspond to oxygens in the sulfonic acid groups. The peak at the lower binding energy of 531.4 eV originates from oxygens that are double bonded to sulfur, whereas the peak at the higher binding energy corresponds to the hydroxyl oxygens. [64]

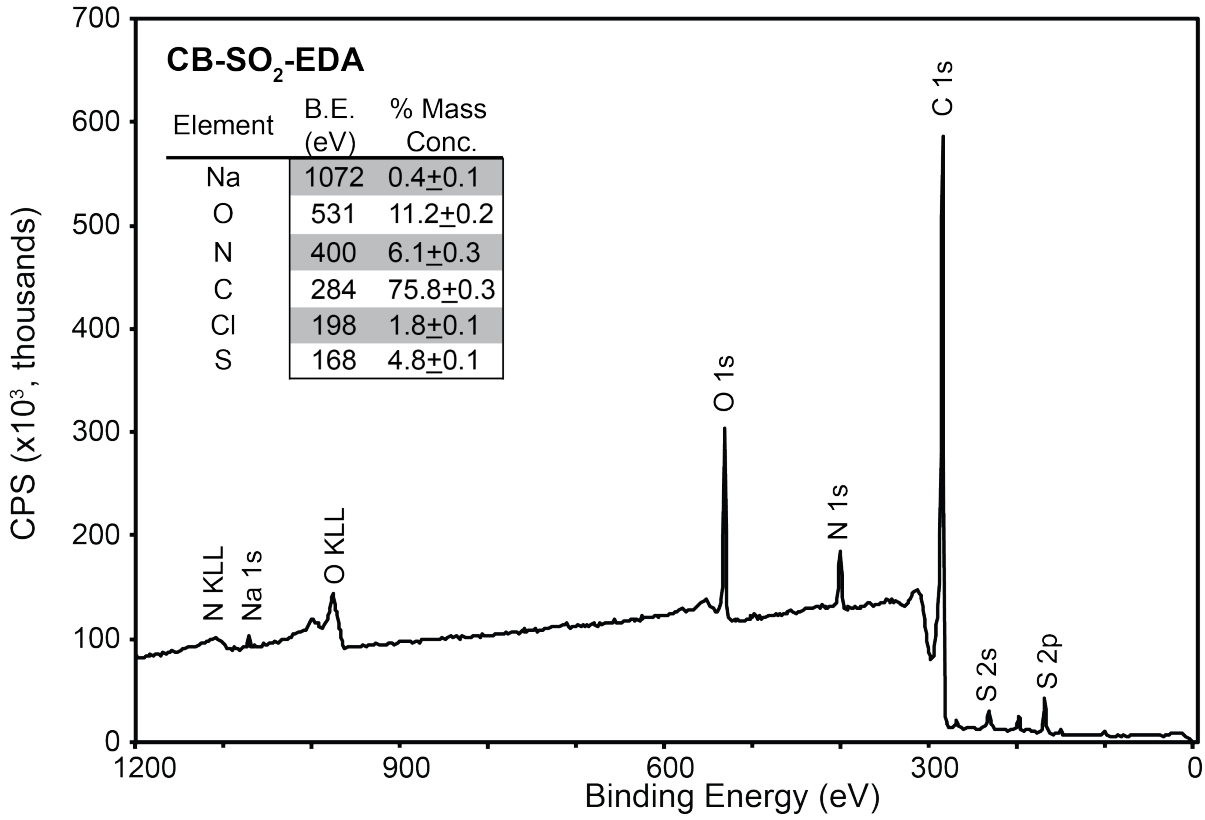

Figure 3.18: Wide-survey XP spectrum for CB-SO_2-EDA.

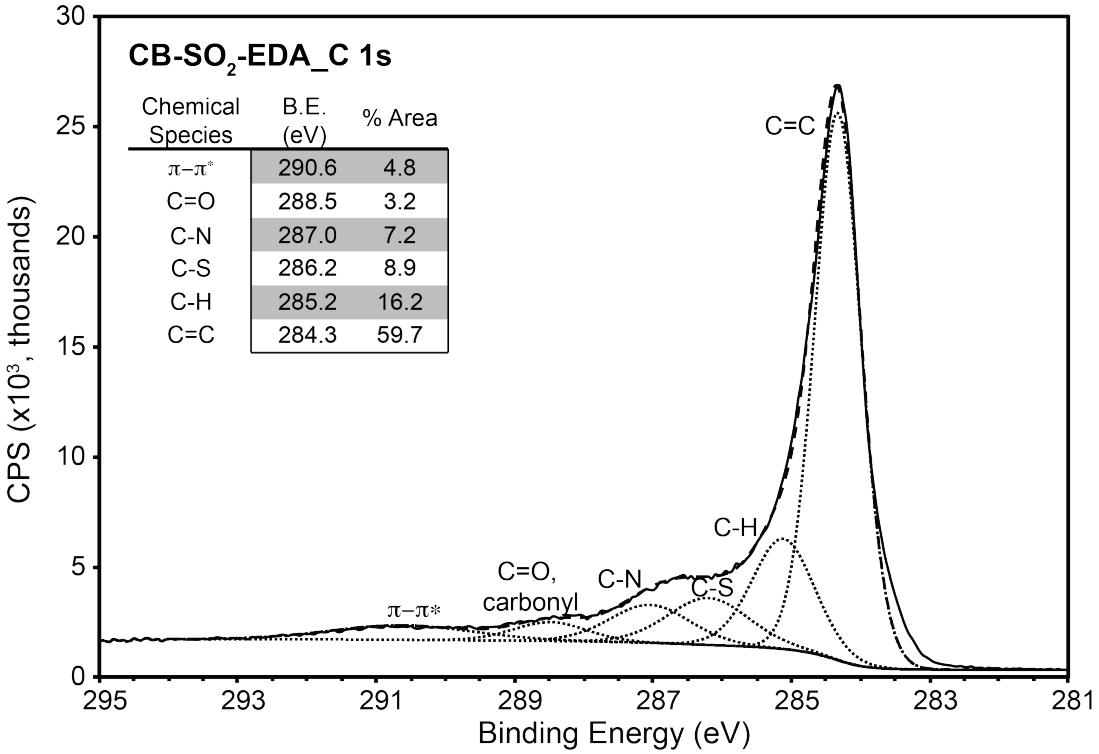
CB-SO2-EDA_C 1s
Chemical Species
B.E. (eV)
% Area
π–π*
290.6
4.8
C=O
288.5
3.2
C-N
287.0
7.2
C-S
286.2
8.9
C-H
285.2
16.2
C=C
284.3
59.7
C=C
C-H
C-S
C-N
C=O, carbonyl
π–π*
CPS (x10³, thousands)
Binding Energy (eV)

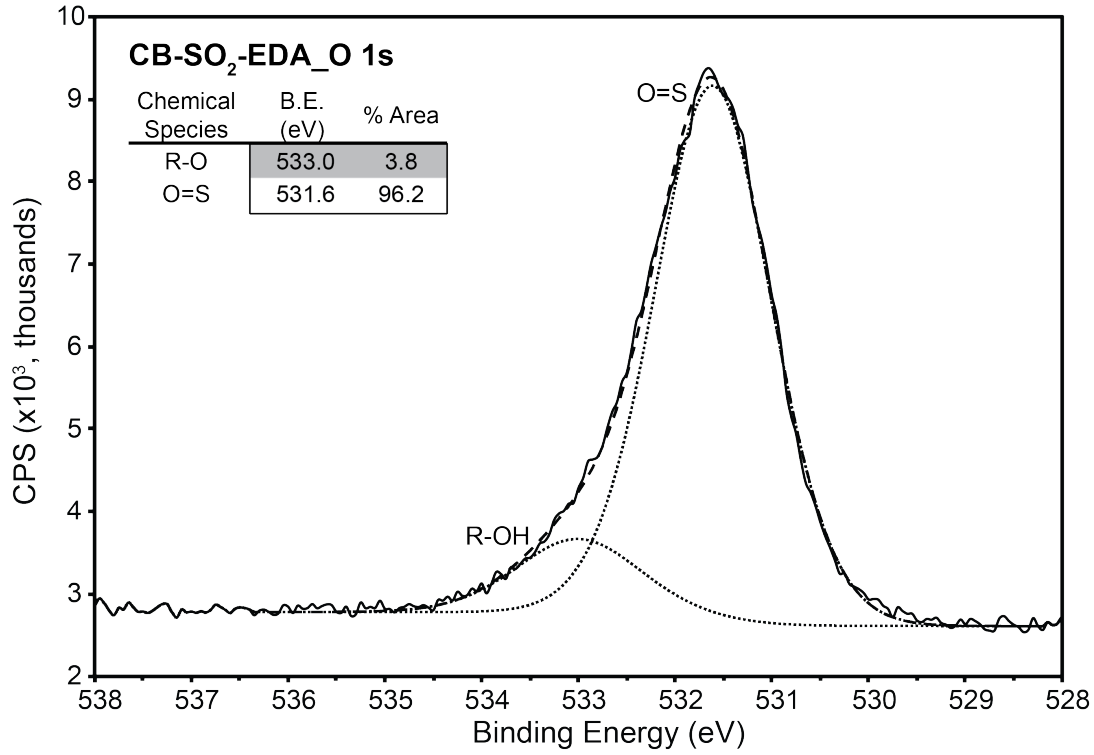
CB-SO2-EDA_O 1s
Chemical Species
B.E. (eV)
% Area
R-O
533.0
3.8
O=S
531.6
96.2
O=S
R-OH
CPS (x10³, thousands)
Binding Energy (eV)

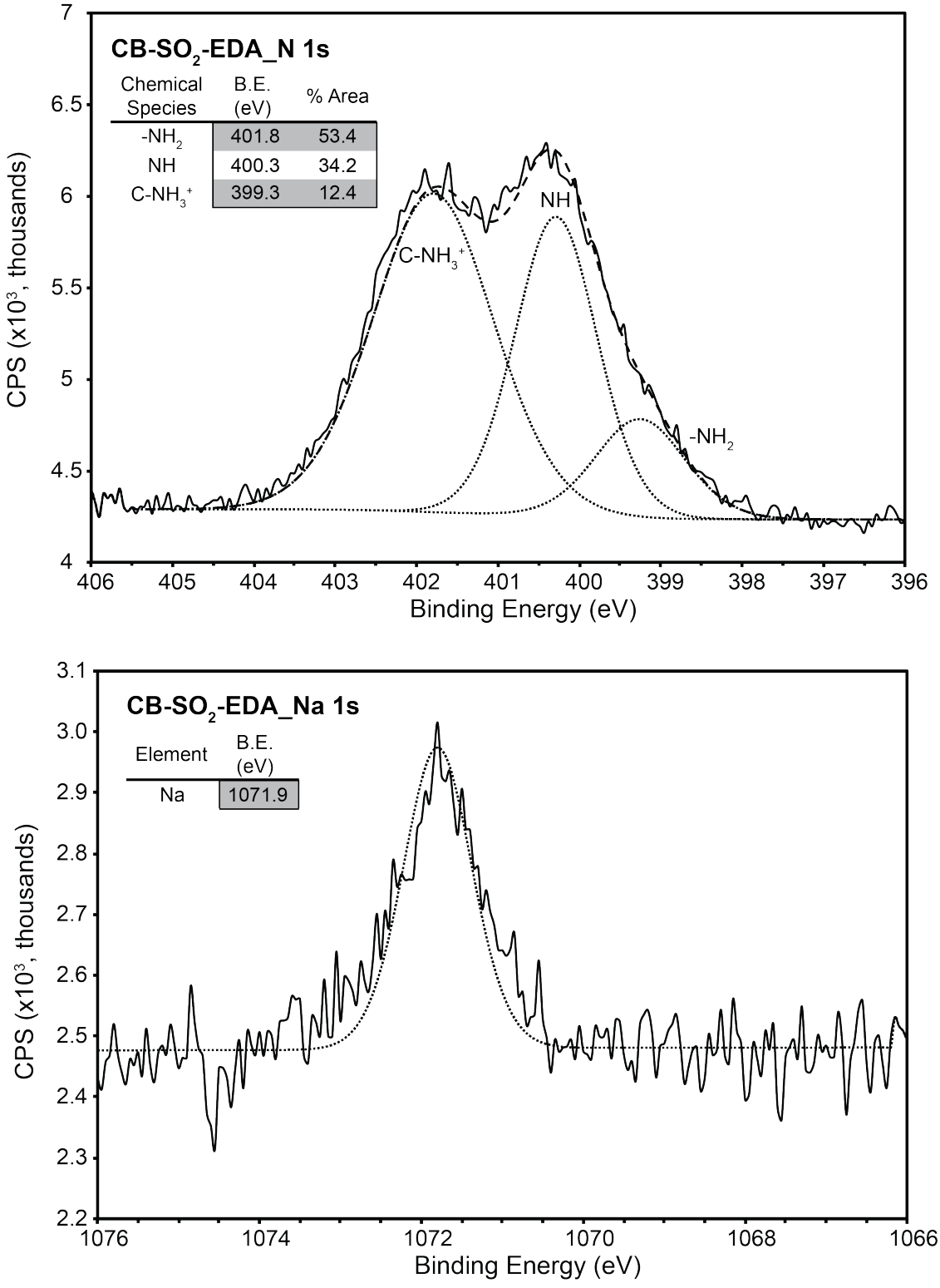

Figure 3.19: High-resolution C1s, O1s, N1s, Na1s XP spectra for CB-SO_2-EDA.

In the case of CB-SO_2-EDA, the peak centered on 401 eV, attributed to N1s, indicates a considerable degree of surface modification with EDA. The XP N1s spectrum, which was further deconvoluted into three components, confirms the formation of amine and amide groups on the CB-SO_2-EDA surface. [65] The N1s energy region is well fitted into three binding energy peaks at 399.3 eV, 400.3 eV, and 401.8 eV, which are attributed to the C-NH_2, C-NH, and protonated nitrogen atoms of the terminal primary amine groups of EDA. [66, 67] The shoulder in the N1s region at 401.8eV is most likely the result of a small amount of the terminal amines that have acquired a proton during the rinsing procedure. [68, 69] The broad C1s peak envelope clearly demonstrates that the carbon atoms are situated in different chemical environments. A shift in the C1s spectra can also be seen after the reaction with EDA along with the appearance of a new peak at 287.0 eV, which was respectively assigned to C-N bonds. [70, 71]

3.4.4 Raman Spectral Data and Analysis

Raman spectroscopy was used to determine the degree of functionalization. [72] Raman spectra for the carbon samples displays two main peaks: at ~1333 cm^{-1} (D band), at ~1551 cm^{-1} (G band), and a broad peak centered at ~2800 cm^{-1} (G' band) attributed to the overtone of the D band.

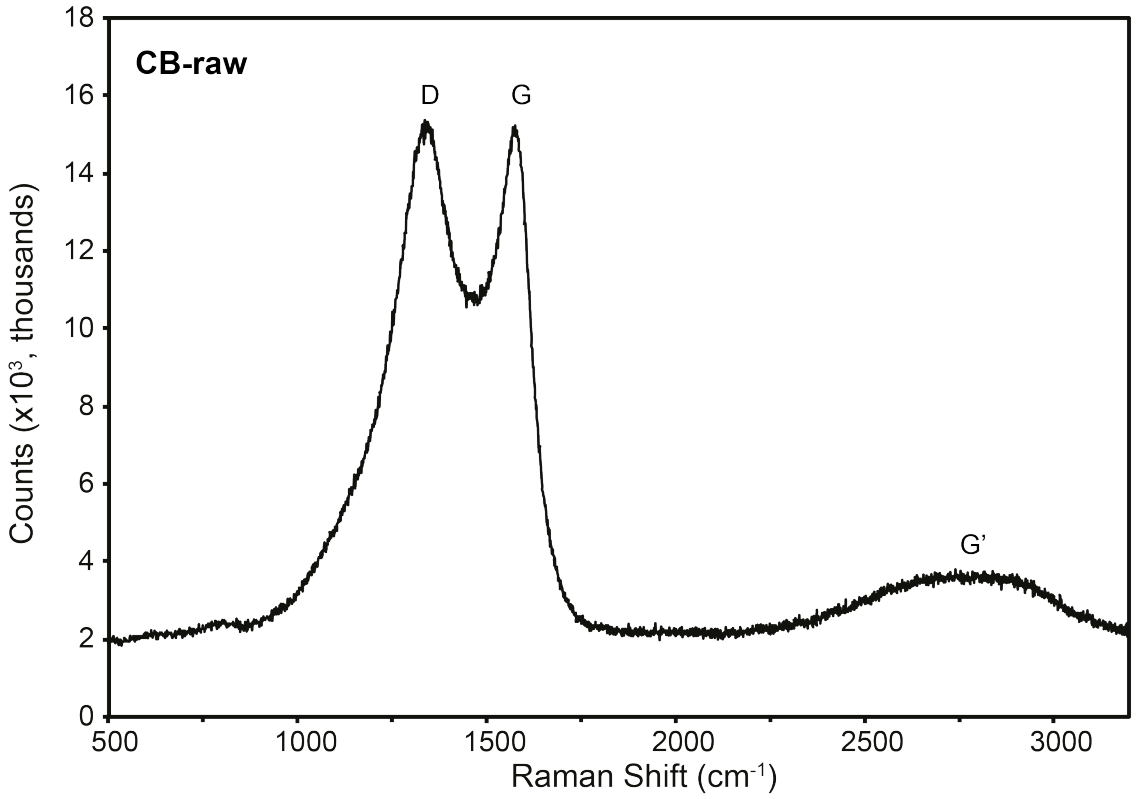

Figure 3.20: Raman Spectrum of unmodified CB-raw.

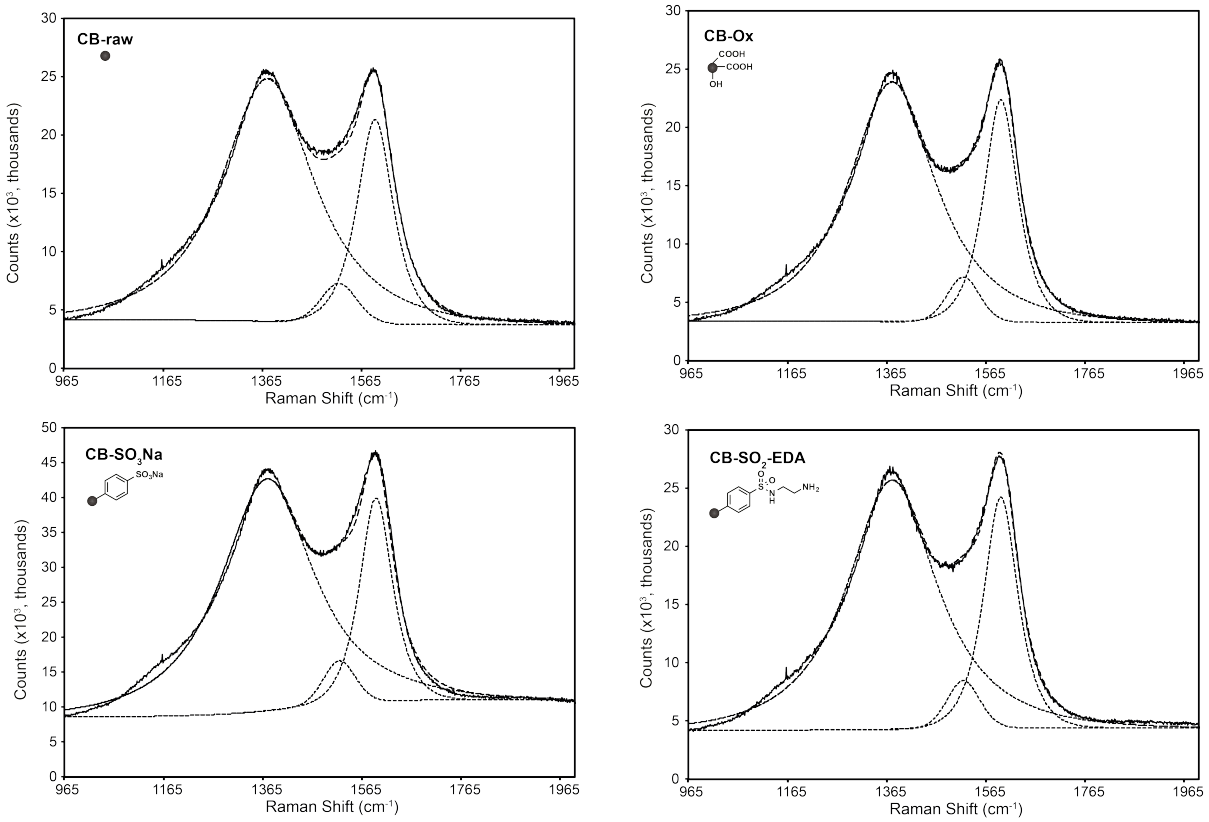

Figure 3.21: Deconvolution of the D and G peaks of CB-raw, CB-Ox, CB-SO_3Na, and CB-SO_2-EDA.

Increased area of the D-band, representing structural disorder or deficit that breaks the transition symmetry, supports covalent surface modification as shown in Table 3.1. [73] Correspondingly, the G-band corresponds to the planar configuration of sp^2 bonded carbon (stretching in the basal plane). [73] An increased area of the G-band could indicate the restoration of the pi-conjugated electronic network as seen when benzene rings are attached to the surface.

NP	% Area of D peak (1375 cm^{-1})	% Area of G peak (1599 cm^{-1})	ID/IG
CB-raw	76.3	23.7	3.21
CB-Ox	74.4	25.5	2.91
CB-SO_3Na	77.2	22.8	3.38
CB-SO_2-EDA	75.0	25.0	2.99

Table 3.1: Comparison of D and G peaks between unmodified and modified CB samples.

3.4.5 Mathematica Analysis

Reaction results are recorded in voltage by the mass flow meter, and in percent CO_2 by the CO_2 meter. Using Mathematica, the flow-rate data and the CO_2 percentage are converted to a plot of CO_2 release (mL/s) vs. time (s). Based on the shape of the flow rate data, the photothermal-enhanced rate of CO_2 release is evident. After converging the flow data with the percentage of released CO_2, two absolute parameters are recorded: the total mass of CO_2 release and the time it takes to reach half the maximum of CO_2 released. By integrating the area under the curve as shown in Figure 3.22, the total amount of CO_2 released.

```
DateConvert[list_] := Module[{dt = 0, tab},
  dt = Table[DateList[list[[i, 1]]], {i, 1, Length[list]}];
  tab = Table[{dt[[i, 4]] * 60 * 60 + dt[[i, 5]] * 60 + dt[[i, 6]] +
       (dt[[i, 3]] * 24 * 60 * 60 - dt[[1, 3]] * 24 * 60 * 60) / 2 - dt[[1, 4]] * 60 * 60 -
       dt[[1, 5]] * 60 - dt[[1, 6]] + 0, N[list[[i, 2]] / 10 000]}, {i, 1, Length[list]}];
  tab]

Clear[findAllRoots]
SyntaxInformation[findAllRoots] = {"LocalVariables" → {"Plot", {2, 2}},
    "ArgumentsPattern" → {_, _, OptionsPattern[]}};
SetAttributes[findAllRoots, HoldAll];

Options[findAllRoots] = Join[{"ShowPlot" → False, PlotRange → All},
   FilterRules[Options[Plot], Except[PlotRange]]];

findAllRoots[fn_, {l_, lmin_, lmax_}, opts : OptionsPattern[]] :=
 Module[{pl, p, x, localFunction, brackets},
  localFunction = ReleaseHold[Hold[fn] /. l ↦ x];
  If[lmin ≠ lmax, pl = Plot[localFunction, {x, lmin, lmax},
     Evaluate@FilterRules[Join[{opts}, Options[findAllRoots]], Options[Plot]]];
   p = Cases[pl, Line[{x__}] ↦ x, Infinity];
   If[OptionValue["ShowPlot"],
    Print[Show[pl, PlotLabel → "Finding roots for this function",
      ImageSize → 200, BaseStyle → {FontSize → 8}]]], p = {}];
  brackets = Map[First, Select[(*This Split trick pretends that two points on
       the curve are "equal" if the function values have _opposite _ sign.Pairs
       of such sign-changes form the brackets for the subsequent FindRoot*)
     Split[p, Sign[Last[#2]] == -Sign[Last[#1]] &], Length[#1] == 2 &], {2}];
  x /. Apply[FindRoot[localFunction == 0, {x, ##1}] &, brackets, {1}] /. x → {}
 ]

flowdat =
  Import["C:\\Users\\User\\Desktop\\Data\\ConvertedFlow\\SAG-I-89-02-flow.CSV"];
cbdat = Drop[Import["C:\\Users\\User\\Desktop\\Data\\CO2Meter\\SAG-I-89-02.csv"],
   5];
cbdat = DateConvert[%];
ListPlot[cbdat, PlotRange → All]
```

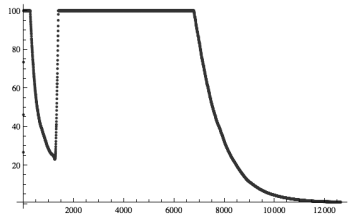


```
cbint = Interpolation[MovingAverage[cbdat, 2]][t]
flowdatt = MovingAverage[Flatten[flowdat], 60] * 1 / 5 * 50;
flowdat2 = Table[{N[i / 60], flowdatt[[i]]}, {i, 1, Length[flowdatt]}];
flowdatint = Interpolation[flowdat2][t]
flowadjust = flowdatint * 0.739 * cbint / 100;
```

InterpolatingFunction[{{1.5, 12 637.5}}, <>][t]

InterpolatingFunction[{{0.0166667, 12 599.}}, <>][t]

```
Plot[flowdatint, {t, 00, 12 000}, PlotRange → {-1.5, 10}]
Plot[flowadjust, {t, 000, 12 000}, PlotRange → {-1.5, 10}]
```

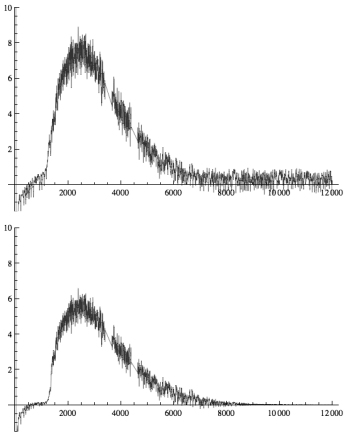


```
total g desorbed = NIntegrate[flowadjust, {t, 400, 10 000}] / 60 / 1 000 000 * 1977
g2 = % / 2
```

0.522041

0.26102

```
gco2 = NIntegrate[flowadjust, {t, 400, 3020}] / 60 / 1 000 000 * 1977
t2 = 3020 - 400
efficiency = (2.2704 * t2) / (g2 / 44.01) * 3000 / 1500
```

0.261175

2620

2.00591×10^6

Figure 3.22: Mathematica Post-Analysis Coding.

Chapter 4

Conclusions

4.1 Photothermal CO_2 Desorption

We demonstrate a new potential energy source for carbon capture and release technologies by regenerating capture fluids using actinic light and carbon black nanoparticles. We report that increased nanoparticle concentration and increased initial capture fluid temperatures resulted in higher regeneration efficiencies. These photothermal nanoparticles could be incorporated, at low loading levels, into CO_2 capture fluids without affecting chemical absorption. Fossil fuels remain inexpensive and this approach might serve as a temporary stop-gap as renewable energy technologies continue to mature. The use of photothermal nanoparticles might aid in the integration of solar energy with CO_2 capture technologies as an economical intermediate. The incorporation of the nanoparticles enables the use of sunlight, instead of steam, to regenerate the capture fluid. Our future work will focus on understanding the basic phenomenon of photothermal gas regeneration, reducing the aggregation of nanoparticles, and optimizing system geometry for light absorption.

4.2 Covalent Surface Modification of CB and Use as CO_2 Capture Nanofluid

This study demonstrates that the surface of CB can be covalently modified to incorporate sulfonamides, which improve the release of CO_2 from MEA ~70% more than the unmodified CB-raw. Covalently modifying the surface of CB was confirmed by the loss of organic groups at high temperatures (>250 °C) as indicated by TGA, and as identified by both FTIR and XPS analysis.

The incorporation of nanofluids into carbon capture and release would enable the use of sunlight, rather than steam, to regenerate the capture fluid at lower bulk temperatures. Photothermal release of CO_2 addresses the high energy costs associated with regenerating capture fluids, which prohibit widespread commercial implementation. Because this method has great potential for industrial applications, as it uses economically available materials and alternative energy sources, it is important to understand this process. By investigating surface functionality of CB, we make progress in exploring how photothermal nanofluids can be enhanced to more efficiently perform separations processes. Carbon capture nanofluids with modified CB showed increased total release of CO_2. Surface modification affected dispersion properties as a nanofluid, yet there was no influence of changes in aggregate sizes on the photothermal release of CO_2. Our future work focuses on understanding the basic phenomenon and mechanism of photothermal gas release, and optimizing system geometry for light absorption in a scaled implementation.

REFERENCES

[1] US Energy Information Administration. Annual energy outlook 2015. DOE/EIA-0383, 2015.

[2] Intergovernmental Panel on Climate Change. Climate Change 2014: Fifth assessment synthesis report. IPCC, Geneva, Switzerland, 2014.

[3] Herzog HJ. What future for carbon capture and sequestration? Environ Sci Technol 2001;35:148A–53A.

[4] Peeters ANM, Faaij APC, Turkenburg WC. Techno-economic analysis of natural gas combined cycles with postcombustion CO_2 absorption, including a detailed evaluation of the development potential. Int J Greenh Gas Con 2007;1:396–417.

[5] Rochelle GT. Amine scrubbing for CO_2 capture. Science 2009;325:1652–4.

[6] Bottoms RR, Inventor. Process for separating acidic gases. US Patent 1,783,901A. Girdler Corporation, 1930.

[7] Mangalapally HP, Notz R, Hoch S, Asprion N, Sieder G, Garcia H et al. Pilot plant experimental studies of post combustion CO_2 capture by reactive absorption with MEA and new solvents. Energy Procedia 2009;1:963–70.

[8] Moser P, Schmidt S, Wallus S, Ginsberg T, Sieder G, Clausen I, et al. Enhancement and long-term testing of optimized post-combustion capture technology – Results of the second phase of the testing programme at the Niederaussem pilot plant. Energy Procedia 2013;37:2377–88.

[9] Kittel J, Idem R, Gelowitz D, Tontiwachwuthikul P, Parrain G, Bonneau A. Corrision in MEA units for CO_2 capture: pilot plant studies. Energy Procedia 2009;1:791–7.

[10] Abu-Zahra MRM, Schneiders LHJ, Niederer JPM, Feron PHM, Versteeg GF. CO_2 capture from power plants. Part I: A parametric study of the technical performance based on monoethanolamine. Int J Greenh Gas Con 2007;1:37–46.

[11] Dumee L, Scholes C, Stevens G, Kentish S. Purification of aqueous amine solvents used in post combustion CO2 capture: A review. Int J Greenh Gas Con 2012;10:443–55.

[12] Aaron D, Tsouris C. Separation of CO_2 from Flue Gas: A Review. Separation Science and Technology 2005;40:321–48.

[13] Rao AB, Rubin ES. A technical, economic, and environmental assessment of amine-based CO_2 capture technology for power plant greenhouse gas control. Environ Sci Technol 2002;36:4467–75.

[14] CSIRO – Advanced Coal Technology Porfolio. Environmental impacts of amine-based CO_2 post-combustion capture process report. CSIRO Energy Technology, 2012.

[15] Moser P, Schmidt S, Sieder G, Garcia H, Stoffregen T. Performance of MEA in a long-term test at the post-combustion capture pilot plant in Niederaussem. Int J Greenh Gas Con 2011;5:620–7.

[16] Luzzi A, Lovegrove K. Solar thermal power generation. Encyclopedia of Energy 2004;5,669–83.

[17] Neumann O, Urban AS, Day J, Lal S, Nordlander P, Halas NJ. Solar vapor generation enabled by nanoparticles. ACS Nano 2013;7:42–9.

[18] Neumann O, Feronti C, Neumann AD, Dong A, Schell K, Lu B, et al. Compact solar autoclave based on steam generation using broadband light-harvesting nanoparticles. Proc Natl Acad Sci 2013;110:11677–81.

[19] Hogan NJ, Urban AS, Ayala-Orozco C, Pimpinelli A, Nordlander P, Halas NJ. Nanoparticles heat through light localization. Nano Lett 2014;14:4640–45.

[20] Fang Z, Zhen YR, Neumann O, Polman A, Garcia de Abajo FJ, Nordlander P, et al. Evolution of light-induced vapor generation at a liquid-immersed metallic nanoparticle. Nano Lett 2013;13:1736–42.

[21] Gao Y, Yuan Z, Gao S. Semiclassical approach to plasmon-electron coupling and Landau damping of surface plasmons. J Chem Phys 2011;134:134702.

[22] Baffou G, Quidant R. Nanoplasmonics for chemistry. Chem Soc Rev 2014;43:3898–907.

[23] Lal S, Clare SE, Halas NJ. Nanoshell-enabled photothermal cancer therapy: impending clinical impact. Acc Chem Res 2008;41:1842–51.

[24] Huang X, El-Sayed IH, Qian W, El-Sayed MA. Cancer cell imaging and photothermal therapy in the near-infrared region by using gold nanorods. J Am Chem Soc 2006;128: 2115–20.

[25] Skirtach AG, Dejugnat C, Braun D, Susha AS, Rogach AL Mohwald H, et al. The role of metal nanoparticles in remote release of encapsulated materials. Nano Lett 2005;5:1371–7.

[26] Boyer D, Tamarat P, Maali A, Lounis B, Orrit M. Photothermal imaging of nanometer-sized metal particles among scatters. Science 2002, 297;1160–3.

[27] Asadirad AM, Erno Z, Branda NR. Photothermal release of singlet oxygen from gold nanoparticles. Chem Commun 2013;49:5639–41.

[28] Haas KM, Lear BJ. Degradation of polypropylene carbonate through plasmonic heating. Nanoscale 2013;5:5247–51.

[29] Fasciani C, Bueno Alejo, CJ, Grenier M, Netto-Ferreira JC, Scaiano JC. High-temperature organic reactions at room temperature using plasmon excitation: Decomposition of dicumyl peroxide. Org Lett 2011;13:204–7.

[30] Liu Y, Yu S, Feng R, Bernard A, Liu Y, Zhang Y, et al. A bioinspired, reusable, paper-based system for high-performance large-scale evaporation. Adv Mater 2015;27:2768–74.

[31] Govorov AO, Richardson HH. Generating heat with metal nanoparticles. Nano Today 2007;2:30–8.

[32] Ni G, Miljkovic N, Ghasemi H, Huang X, Boriskina SV, Lin C, et al. Volumetric solar heating of nanofluids for direct vapor generation. Nano Energy 2015;17:290–301.

[33] Haas KM, Lear BJ. Billion-fold rate enhancement of urethane polymerization via the photothermal effect of plasmonic gold nanoparticles. Chem Sci 2015;6:6462–7.

[34] Moon HK, Lee SH, Choi HC. In vivo near-infrared mediated tumor destruction by photothermal effect of carbon nanotubes. ACS Nano 2009;3:3707–13.

[35] Han D, Meng Z, Wu D, Zhang C, Zhu H. Thermal properties of carbon black aqueous nanofluids for solar absorption. Nanoscale Res Lett 2011;6:457.

[36] Baral S, Green AJ, Livshits MY, Govorov AO, Richardson HH. Comparison of vapor formation of water at the solid/water interface to colloidal solutions using optically excited gold nanostructures. ACS Nano 2014;8:1439–48.

[37] Nguyen DT, Truong R, Lee R, Goetz SA, Esser-Kahn AP. Photothermal release of CO_2 from capture solutions using nanoparticles. Energy Environ Sci 2014;7:2603–7.

[38] Tong D, Trusler JPM, Maitland GC, Gibbins J, Fennell PS. Solubility of carbon dioxide in aqueous solution of monoethanolamine or 2-amino-2-methyl-1-propanol: Experimental measurements and modeling. Int J Greenh Gas Con 2012;6:37–47.

[39] Nguyen, DT. Novel Approaches to carbon capture: Biomimetic absorption and solar desorption. Irvine CA USA, University of California Irvine, PhD thesis, 2015.

[40] Fisher KS, Beitler C, Rueter C, Searcy K, Rochelle G, Jassim M. Integrating MEA regeneration with CO_2 compression and peaking to reduce CO_2 capture costs. Technical Report DOE/ER/84111, USDOE Office of Fossil Energy (FE) Report DOE/ER/84111, June 2005.

[41] Cohen SM, Webber ME, and Rochelle GT. Utilizing solar thermal energy for post-combustion CO_2 capture. J Energy Power Eng 2011,5:195–208.

[42] Price H, Lupfert E, Kearney D, Zarza E, Gilbert Cohen G, Gee R, et al. Advances in parabolic trough solar power technology. J Sol Energy Eng 2002;124:109–25.

[43] Jiang J, Oberdörster G, Biswas P. Characterization of size, surface charge, and agglomeration sate of nanoparticle dispersions for toxicological studies. J Nanopart Res 2009;11:77–89.

[44] Vicentini FC, Ravanini AE, Figueiredo-Filho LCS, Iniesta J, Banks CE, Fatibello-Filho, O. Imparting improvements in electrochemical sensors: Evaluation of different carbon blacks that give rise to significant improvement in the performance of electroanalytical sensing platforms. Electrochimica Acta 2015;157:125–33.

[45] Stoeckli HF. Microporous carbons and their characterization: the present state of the art. Carbon 1990;28:1–6.

[46] Zhang L, Zhang F, Yang X, Long G, Wu Y, Zhang T, et al. Porous 3D graphene-based bulk materials with exceptional high surface area and excellent conductivity for supercapacitors. Sci Reports 2013;3:1408.

[47] Bertoti I, Mohai M, Laszlo K. Surface modification of graphene and graphite by nitrogen plasma: Determination of chemical state alterations and assignments by quantitative X-ray photoelectron spectroscopy. Carbon 2015;84:185–96.

[48] Soares MCF, Viana MM, Schaefer ZL, Gangoli VS, Cheng Y, Caliman V, et al. Surface modification of carbon black nanoparticles by dodecylamine: Thermal stability and phase transfer in brine medium. Carbon 2014;72:287–95.

[49] Gomez-Serrano V, Piriz-Almeida F, Duran-Valle CJ, Pastor-Villegas J. Formation of oxygen structures by air activation. A study by FT-IR spectroscopy. Carbon 1999;37:1517–28.

[50] Tan X, Liu Y, Zeng G, Wang X, Hu X, Gu Y, et al. Application of biochar for the removal of pollutants from aqueous solutions. Chemosphere 2015;125:70–85.

[51] Zawadzki J. Infrared spectroscopy in surface chemistry of carbons. In: Chemistry and physics of carbon, vol. 21, New York, California (USA); Marcel Dekker Inc, American Carbon Society; 1989, p. 147–380.

[52] Zorn G, Baio JE, Weidner T, Migonney V, Castner DG. Characterization of poly(sodium styrene sulfonate) thin films grafted from functionalization titanium surfaces. Langmuir 2011;27:13104–12.

[53] Silverstein RM, Webster FX, Kiemle DJ. Spectrometric Identification of Organic Compounds. 7th ed. NewYork: John Wiley & Sons, Inc; 2005: p. 72–126.

[54] Barbero C, Miras MC, Schnyder B, Haas O, Kotz R. Sulfonated polyaniline films as cation insertion electrodes for battery applications. J Mater Chem 1994;4:1775–83.

[55] Stine R, Ciszek JW, Barlow DE, Lee WK, Robinson JT, Sheehan PE. High-density amine-terminated monolayers formed on fluorinated CVD-grown graphene. Langmuir 2012;28:7957−61.

[56] Li T, Liu Y, Wang S, Zeng G, Zheng B, Wang H, et al. Synthesis and absorption application of amine shield-introduced-released porous chitosan hydrogel beads for removal of acid orange 7 from aqueous solutions. RSC Adv 2015;5:62778–87.

[57] Biniak S, Szymanski G, Siedlewski J, Swiatkowski A. The characterization of activated carbons with oxygen and nitrogen surface groups. Carbon 1997;35:1799–810.

[58] Johnson JE, Belmont JA, Inventors. Modified colored pigments and ink jet inks, inks, and coatings containing modified colored pigments. US patent US 5922118 A, 1999.

[59] Watkins JD, Lawrence K, Taylor JE, James TD, Bull SD, Marken F. Carbon nanoparticle surface electrochemistry: High-density covalent immobilization and pore-reactivity of 9,10-anthraquinone. Electroanalysis 2011;23:1320–24.

[60] Li N, Ma X, Zha Q, Kim K, Chen Y, Song C. Maximizing the number of oxygen-containing functional groups on activated carbon by using ammonium persulfate and improving the temperature-programmed desorption characterization of carbon surface chemistry. Carbon 2011;491:5002–13.

[61] Yoo JE, Lee KS, Garcia A, Tarver J, Gomez ED, Baldwin K, et al. Directly patternable, highly conducting polymers for broad applications in organic electronics. Proc Natl Acad Sci 2010;107:5712–7.

[62] Balachander N, Sukenik CN. Monolayer transformation by nucleophilic substitution: Applications to the creation of new monolayer assemblies. Langmuir 1990;6:1621–7.

[63] Zorn G, Baio JE, Weidner T, Migonney V, Castner DG. Characterization of poly(sodium styrene sulfonate) thin films grafted from functionalization titanium surfaces. Langmuir 2011;27:13104–12.

[64] Greczynski G, Kugler T, Keil M, Osikowicz W, Fahlmman M, Salaneck WR. Photoelectron spectroscopy of thin films of PEDOT-PSS conjugated polymer blend: A mini-review and some new results. J Electron Spectrosc 2001;121:1–17.

[65] Kim KS, Park SJ. Influence of amine-grafted multi-walled carbon nanotubes on physical and rheological properties of PMMA-based nanocomposites. J Solid State Chem 2011;184:3021–7.

[66] Wanger CD, Riggs WM, Davis LE, Moulder J. Handbook of X-Ray photoelectron spectroscopy. 1st ed. Minnesota: Perkin-Elmer Corp; 1979.

[67] Rong M, Lin L, Song X, Wang Y, Zhong Y, Yan J, et al. Fluorescence sensing of Cr(VI) and ascorbic acid using graphitic carbon nitride nanosheets as a fluorescent "switch." Biosensors and Bioelectronics 2015;68:210–7.

[68] Stine R, Ciszek JW, Barlow DE, Lee WK, Robinson JT, Sheehan PE. High-density amine-terminated monolayers formed on fluorinated CVD-grown graphene. Langmuir 2012;28:7957−61.

[69] Setiawan LD, Baumann H, Gribbin D. Surface studies of keratin fibers and related model compounds using ESCA. Surf Interface Anal 1985;7:188−95.

[70] Zhu L, Lu Y, Wang Y, Zhang L, Wang W. Preparation and characterization of dopamine-decorated hydrophilic carbon black. Appl Surf Sci 2012;258:5387–93.

[71] Xu W, Wang S, Liu Y, Zeng G, Zheng B, Tan X, et al. Tartaric acid modified Pleurotus ostreatus for enhanced removal of Cr(VI) ions from aqueous solution: characteristics and mechanisms. RSC Adv 2015;5:24009–15.

[72] Graupner R. Raman spectroscopy of covalently functionalized single-wall carbon nanotubes. J Raman Spectrosc 2007;38:673–83.

[73] Bokobza L, Bruneel JL, Couzi M. Raman spectroscopic investigation of carbon-based materials and their composites. Comparison between carbon nanotubes and carbon black. Chemical Physics Letters 2013;590:153–9.